

Mechanically-Guided Structural Designs in Stretchable Inorganic Electronics

Zhaoguo Xue, Honglie Song, John A. Rogers,* Yihui Zhang,* and Yonggang Huang*

Over the past decade, the area of stretchable inorganic electronics has evolved very rapidly, in part because the results have opened up a series of unprecedented applications with broad interest and potential for impact, especially in bio-integrated systems. Low modulus mechanics and the ability to accommodate extreme mechanical deformations, especially high levels of stretching, represent key defining characteristics. Most existing studies exploit structural material designs to achieve these properties, through the integration of hard inorganic electronic components configured into strategic 2D/3D geometries onto patterned soft substrates. The diverse structural geometries developed for stretchable inorganic electronics are summarized, covering the designs of functional devices and soft substrates, with a focus on fundamental principles, design approaches, and system demonstrations. Strategies that allow spatial integration of 3D stretchable device layouts are also highlighted. Finally, perspectives on the remaining challenges and open opportunities are provided.

but remove the constraints of rigid, brittle, planar, wafer substrates, through the strategic integration with soft elastomers.^[1–14] Compared with the conventional rigid devices, stretchable inorganic electronics not only allow large deformations without degradation in electronic performances, but also yield conformal integration with the complex surfaces of tissues of the human body.^[8,15–20] Due to these unique advantages, stretchable inorganic electronics technologies significantly broaden the application areas of conventional electronics, and also enable novel uses in health monitoring, advanced human–machine interfaces and internet of things, such as epidermal electronics,^[21–25] curvilinear electronics,^[26–28] deformable optoelectronics,^[29–34] transient electronics,^[35–37] and many other bioelectronic systems.^[38–40]

With a series of rapid developments over

1. Introduction

Some of the most useful forms of stretchable inorganic electronics leverage mature planar semiconductor technologies,

more than a dozen of years, stretchable inorganic electronic systems now define a well-recognized and active field of study, encompassing a diverse range of fundamental and applied topics,^[41–53] including, for example, a collection of unusual material/structure designs and techniques to integrate hard inorganic semiconductor components and geometrically structural interconnects in optimized layouts onto patterned soft substrates.^[7,54,55]

Dr. Z. Xue, Dr. H. Song, Prof. Y. Zhang
Applied Mechanics Laboratory
Department of Engineering Mechanics
Center for Flexible Electronics Technology
Tsinghua University
Beijing 100084, China
E-mail: yihuizhang@tsinghua.edu.cn

Prof. J. A. Rogers
Departments of Materials Science and Engineering, Biomedical Engineering, Neurological Surgery, Chemistry, Mechanical Engineering Electrical Engineering and Computer Science
Simpson Querrey Institute and Feinberg Medical School
Center for Bio-Integrated Electronics
Northwestern University
Evanston, IL 60208, USA
E-mail: jrogers@northwestern.edu

Prof. Y. Huang
Departments of Mechanical Engineering
Civil and Environmental Engineering
and Materials Science and Engineering
Center for Bio-Integrated Electronics
Northwestern University
Evanston, IL 60208, USA
E-mail: y-huang@northwestern.edu

 The ORCID identification number(s) for the author(s) of this article can be found under <https://doi.org/10.1002/adma.201902254>.

Stretchable electronics have achieved high levels of sophistication largely through the use of inorganic active materials. According to the utility of different conductive materials, stretchable inorganic electronics can be classified into three categories, including those based on the composite stretchable conductors, liquid metals, and structured semiconductors/metals.^[49,56–58] In the first category, novel nanomaterials dispersed into a polymer matrices form composite films or fibers, by coating, dipping, printing, and electrospinning. Various nanomaterials have been exploited in this context, including metal nanoparticles, nanowires, nanoflakes, and the allotropes of carbon (carbon nanotubes, graphene, and carbon blacks).^[59–66] A key to this strategy is in maintaining interconnected pathways through these nanomaterials to enable highly conductive channels when the substrate is stretched.^[67–71] Despite great progress, the conductivities of such composites are typically lower than those of conventional metals. The second category of stretchable inorganic conductors relies on liquid metals patterned and encapsulated into channels of elastomeric materials.^[72,73] Such constructs can be bent and stretched to levels beyond those possible with conventional electronic materials.

DOI: 10.1002/adma.201902254

These stretchable designs may facilitate extreme stretchability, while maintaining excellent conductivity.^[74–76] Challenges are in avoiding blockage and fragmentation of liquid metal in the channels during stretching, preventing oxidation over many cycles of deformation, establishing robust, reliable contacts to electronic components and ensuring robust, reliable packaging without leakage. A third category exploits mechanically guided structural designs, which can couple large deformations of architectures formed in inorganic materials and embedded in elastomer substrates, without failure.^[23,75,77–79] Various design principles can support the intimate integration of systems formed using these strategies with the dynamic, curvilinear surfaces of human tissues/organs for new classes of bioelectronics devices. The current review focuses on these concepts and the resulting technologies that they support.

Inorganic semiconductors and metal foils that are directly fabricated or integrated on flexible substrates cannot sustain large levels of stretching that are required in many emerging bio-integrated applications. Here, the main challenge involves effectively reducing the strains in the rigid inorganic electronic materials and metallic interconnects, while accommodating the large applied tensile deformations at the system level. Progress in this area has led to a collection of structural designs in inorganic electronic materials and soft substrates as an effective strategy to address this challenge.^[80–87] In this review, we highlight such structural designs in state-of-the-art inorganic stretchable electronics, covering four important aspects of the design and manufacture, as illustrated in **Figure 1**. The schemes encompass the various strategies based on wavy, island-bridge, fractal, and kirigami structures, with substrates that involve cellular/surface microstructures and curvilinear patterns. In addition, we present structural designs for integration schemes that determine the mechanical and electrical performances of the entire device systems. Finally, we provide perspectives on the remaining challenges and open opportunities in this area.

2. Structural Designs of Devices and Systems

High performance inorganic materials are ubiquitous in modern electronics, but their natural rigidity and brittle character (e.g., the fracture strain of silicon is only $\approx 2\%$) limit the stretchability of the resulting devices. Recent progress shows that structural designs of materials and devices can render inorganic electronics into forms that provide large effective levels of stretchability, while maintaining the high performance electrical properties. This section focuses on discussions of several representative structural designs, including the wavy, “island-bridge,” fractal, and kirigami designs.

2.1. Wavy Designs

High levels of bendability in brittle and rigid inorganic materials have been demonstrated in the extremely thin membranes.^[88,89] **Figure 2a** shows that the thin film materials with the thickness down to nanometers exhibit a unique mechanical bendability. For example, the flexural rigidity of extremely thin silicon (Si) nanomembrane (thickness < 2 nm) is more than 15 orders of



John A. Rogers is the Louis Simpson and Kimberly Querrey Professor of Materials Science and Engineering, Biomedical Engineering, Mechanical Engineering, Electrical Engineering and Computer Science, Chemistry and Neurological Surgery at Northwestern University, where he also serves as

Director of the Center on Bio-Integrated Electronics. Rogers' research focuses on unusual electronic and photonic devices, with an emphasis on bio-integrated and bio-inspired systems.



Yihui Zhang obtained his Ph.D. (2011) in solid mechanics from the Department of Engineering Mechanics at Tsinghua University. Then he worked as a Postdoctoral Fellow from 2011 to 2014 and as a Research Assistant Professor from 2014 to 2015, both at Northwestern University. He joined the Department of

Engineering Mechanics at Tsinghua University in 2015, and was tenured in 2018. His research interests include mechanically guided 3D assembly, unusual soft composite materials, and stretchable electronics.



Yonggang Huang obtained B.S. degree in mechanics from Peking University, China, in 1984, and S.M. and Ph.D. degrees in engineering science from Harvard University in 1987 and 1990, respectively. He is the Walter P. Murphy Professor of Mechanical Engineering, Civil and Environmental Engineering, and Materials

Science and Engineering at Northwestern University. He is interested in mechanics of stretchable and flexible electronics and mechanically guided deterministic 3D assembly.

magnitude smaller than that of its bulk wafer (200 μm).^[90] To further meet the demand for large stretchability in practical applications, specialized structural layouts and mechanical designs are required. The “wavy” designs^[91–93] shown in **Figure 2b** provide a representative example, in which the applied tensile strains of the overall system are accommodated mainly through changes in the amplitudes and wavelengths of the wavy structures.^[94–101]

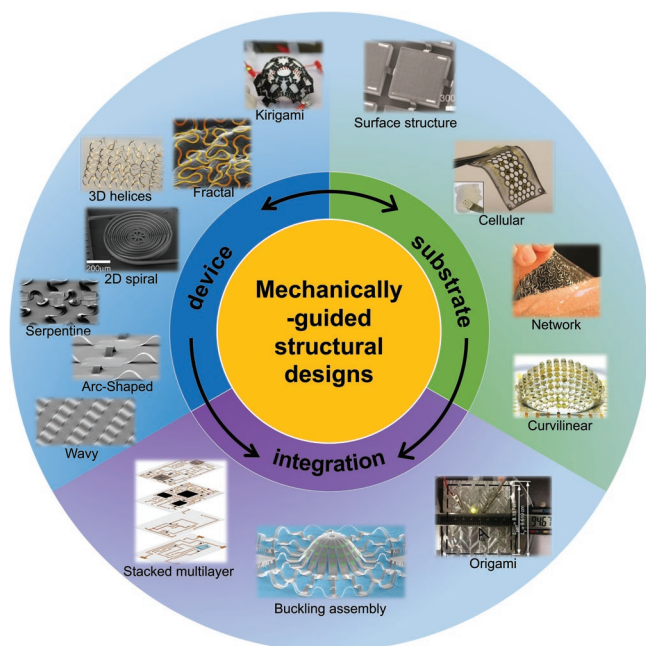


Figure 1. Summary of the review. Strategies of mechanically guided structural designs in inorganic stretchable electronics. I) Structural designs of devices and systems, including wavy designs, island-bridge designs (e.g., arc-shaped, serpentine, 2D spiral, 3D helical), fractal-inspired designs and kirigami strategy. Wavy: Reproduced with permission.^[102] Copyright 2006, American Association for the Advancement of Science. Arc-shaped interconnects: Reproduced with permission.^[26] Copyright 2008, Nature Publishing Group. Serpentine interconnects: Reproduced with permission.^[41] Copyright 2008, National Academy of Sciences. 2D spiral interconnects: Reproduced with permission.^[136] Copyright 2007, IEEE. 3D helical interconnects: Reproduced with permission.^[142] Copyright 2017, Nature Publishing Group. Fractal-inspired design: Reproduced with permission.^[154] Copyright 2014, Nature Publishing Group. Kirigami strategy: Reproduced with permission.^[44] Copyright 2014, National Academy of Sciences. II) Structural designs of substrate, by introducing surface structure designs, cellular designs, and curvilinear designs. Surface structure: Reproduced with permission.^[176] Copyright 2011, Wiley-VCH. Cellular substrate: Reproduced with permission.^[179] Copyright 2017, Wiley-VCH. Network substrate: Reproduced with permission.^[136] Copyright 2015, Nature Publishing Group. Curvilinear: Reproduced with permission.^[27] Copyright 2013, Nature Publishing Group. III) Structural designs for spatial integration of device systems by strategies of folding-based origami, buckling-guided 3D assembly, and stacked multilayer designs. Origami strategy: Reproduced with permission.^[42] Copyright 2014, Nature Publishing Group. Buckling assembly: Reproduced with permission.^[231] Copyright 2018, Nature Publishing Group. Stacked multilayer: Reproduced with permission.^[246] Copyright 2018, Nature Publishing Group.

Two strategies have been demonstrated to produce wavy structures on an elastomeric substrate, as illustrated in Figure 2c. Here, ribbon-shaped thin films are transferred onto a prestretched polydimethylsiloxane (PDMS) substrate, where the surface chemical treatment enables strong bonding either throughout the full lengths of the ribbons or at selective sites. After releasing the prestrain, the thin films are compressed into wavy structures,^[45,102–105] as shown in Figure 2d,e, corresponding to these two different bonding strategies.

For the full bonding strategy, many mechanics models have been developed to predict the configurations of the wavy ribbon structures, as well as their stretchabilities.^[97,100,106,107] In the

regime of small deformations ($\epsilon_{pre} \leq 5\%$), an energetic approach based on the small-deformation theory was developed to determine the buckled shapes, in which the out-of-plane displacement of the ribbon is assumed as a sinusoidal profile. In the regime of large deformations ($\epsilon_{pre} > 5\%$), the effect of the finite deformation in the elastomeric substrate must be considered. Jiang et al.^[103] and Song et al.^[108] developed analytic models in the framework of finite deformation theory, taking into account the finite geometry change with different strain-free states for the thin film and substrate, the finite strain (Green strain) with a nonlinear strain-displacement relationship for the substrate, and a nonlinear constitutive model (neo-Hookean) for the substrate. These models yield an analytic solution to the wavelength and amplitude, as given by

$$\lambda_{app} = \frac{2\pi h_f (1 + \epsilon_{app})}{(1 + \epsilon_{pre})(1 + \epsilon_{app} + \xi)^{1/3}} \left(\frac{\bar{E}_f}{3\bar{E}_s} \right)^{1/3} \quad (1)$$

$$\text{and } A_{app} = \frac{h_f \sqrt{(\epsilon_{pre} - \epsilon_{app})/\epsilon_c - 1}}{(\sqrt{1 + \epsilon_{pre}})(1 + \epsilon_{app} + \xi)^{1/3}}$$

where the subscripts f and s represent the thin film and the elastic substrate, respectively; h_f is the thickness of thin film; $\epsilon_c = \frac{1}{4} \left(\frac{\bar{E}_s}{3\bar{E}_f} \right)^{2/3}$ is the critical strain for the buckling to occur and is extremely small (e.g., 0.034% for Si/PDMS system); $\bar{E} = \frac{E}{(1 - \nu^2)}$ is the plane-strain modulus with E and ν denoting the Young's modulus and Poisson ratio; and $\xi = 5(\epsilon_{pre} - \epsilon_{app})\epsilon_{pre}(1 + \epsilon_{pre})/32$.

Comparison between the results of experiments and finite element calculations shows the accuracy of Equation (1) (Figure 2f). Since in the buckled thin film system, the thin film strain is usually much smaller than the bending strain, the peak strain ϵ_{peak} can be approximated as

$$\epsilon_{peak} \approx \frac{2\sqrt{(\epsilon_{pre} - \epsilon_{app})\epsilon_c(1 + \epsilon_{app} + \xi)^{1/3}}}{\sqrt{1 + \epsilon_{pre}}} \quad (2)$$

Since the critical strain ϵ_c is extremely small, the peak strain ϵ_{peak} is much smaller than the prestrain ϵ_{pre} .

When a tensile strain is applied to the buckled thin film system, fracture will occur as $\epsilon_{app} = \epsilon_{pre} + \epsilon_{fracture}$ is reached, where ϵ_{pre} is the fracture strain of thin film. The stretchability is $\epsilon_{stretchability} = \epsilon_{pre} + \epsilon_{fracture}$. When a compressive strain is applied to the buckled thin film system, fracture will occur as

$$\epsilon_{app} = \epsilon_{pre} - \frac{\epsilon_{fracture}^2}{4\epsilon_c} \left(1 + \frac{43}{48} \frac{\epsilon_{fracture}^2}{4\epsilon_c} \right) \text{ is reached. Thereby, the compressibility is } \epsilon_{compressibility} = \frac{\epsilon_{fracture}^2}{4\epsilon_c} \left(1 + \frac{43}{48} \frac{\epsilon_{fracture}^2}{4\epsilon_c} \right) - \epsilon_{pre}.$$

These results show that as the prestrain increases, the stretchability of the system increases, and the compressibility deteriorates. It is noteworthy that the stretchability of the system is much larger than the fracture strain ($\approx 2\%$) of Si thin film.

For the selective bonding strategy, as shown in Figure 2e,g, formation of the wavy structure follows from a process of controlled Euler buckling.^[109–112] Here, the bonding sites on the

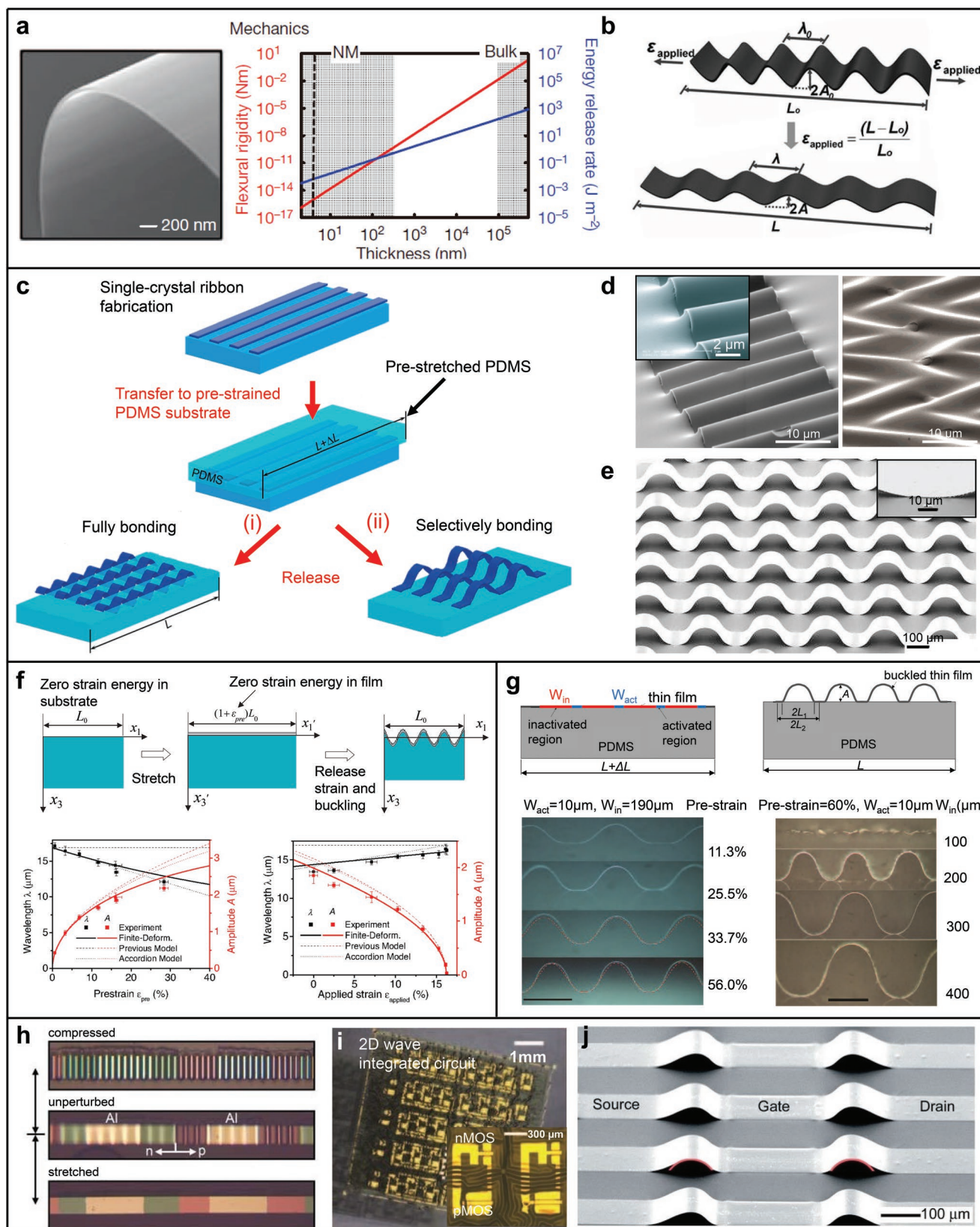


Figure 2. Wavy designs. a) The bendability and the flexural rigidity of thin Si nanomembranes. Reproduced with permission.^[90] Copyright 2011, Nature Publishing Group. b) Schematic illustration of the wavy design of nanomembranes for stretchability. Reproduced with permission.^[91] Copyright 2008, Wiley-VCH. c) Schematic illustration of two different bonding strategies on the elastomeric PDMS substrate for wavy structures, that are fully and

PDMS surface were selectively activated with UV/ozone exposure or by oxygen plasma treatment to allow chemical bonding to thin film upon contact, while the inactivated region adhere by weak van der Waals interactions.^[105] Theoretical analysis shows that the buckling profile can be expressed by a sinusoidal function as

$$w = \begin{cases} w_1 = \frac{1}{2} A \left(1 + \cos \frac{\pi x_1}{2} \right), & -L_1 < x_1 < L_1 \\ w_2 = 0, & L_1 < |x_1| < L_2 \end{cases} \quad (3)$$

where w_1 and w_2 are the profiles of delaminated and bonded parts, A is the buckling amplitude, $2L_1$ is the buckling wavelength, and $2L_2$ is the total length of activated and inactivated regions after relaxation (Figure 2g). Minimization of the total energy gives the buckling amplitude as

$$A = \frac{4}{\pi} \sqrt{L_1 L_2 (\epsilon_{\text{pre}} - \epsilon_c)} \approx \frac{2}{\pi} \frac{\sqrt{W_{\text{in}} (W_{\text{in}} + W_{\text{act}}) \epsilon_{\text{pre}}}}{1 + \epsilon_{\text{pre}}} \quad (4)$$

where $\epsilon_c = h_f^2 \pi^2 / 12 L_1^2$ is the critical strain to trigger the buckling, and is much smaller than the prestrain ϵ_{pre} in most practical applications. This equation suggests that the amplitude is independent of the mechanical properties and the film thickness, and is mainly determined by the prestrain (ϵ_{pre}) and the layout of adhesion sites. Figure 2g shows the profiles of buckled gallium arsenide (GaAs) thin films formed on the PDMS substrate with different ϵ_{pre} and W_{in} , where good agreement between the theoretical predictions and experiment results can be observed.^[112]

The peak strain in the buckled thin film is $\epsilon_{\text{peak}} \approx \pi \frac{h_f}{L_1} \sqrt{\frac{L_2}{L_1}} \epsilon_{\text{pre}}$,

which is typically much smaller than the prestrain. For example, the peak strain is calculated as 0.6% for a 300 nm thick GaAs film buckled on a patterned PDMS substrate with $W_{\text{act}} = 10 \mu\text{m}$, $W_{\text{in}} = 400 \mu\text{m}$, and $\epsilon_{\text{pre}} = 60\%$, which is two orders of magnitude smaller than the prestrain. This behavior ensures large stretchability for devices formed with the selective bonding strategy.

Base on the underlying principles discussed above, the wave designs have been widely exploited in the stretchable inorganic electronics and optoelectronic devices.^[113] In some of the earliest work based on the full bonding strategy, Khang et al.^[102]

demonstrated a stretchable single crystal Si p–n diode on a PDMS substrate (Figure 2h) that remained stable when subjected to the applied strain of –11% (top), 0% (middle), and 11% (bottom). Furthermore, stretchable integrated circuits with biaxial stretchability were realized based on 2D wavy designs, which can function normally under an external stretching along any directions in the plane of the circuit (Figure 2i).^[114] With the selective bonding strategy, metal–semiconductor field-effect transistors (MESFETs) based on controlled buckled GaAs thin films^[45] were demonstrated (Figure 2j), where the wavy GaAs thin film can accommodate a large applied strain of $\approx 20\%$.

2.2. Island-Bridge Designs

To realize highly increased levels of stretchability, beyond those achievable with the wavy designs, the island-bridge design was proposed.^[41] Here, the discrete islands (rigid functional device components) adhered to the flexible substrates are connected by stretchable bridges (electrical interconnects), wherein the islands remain strongly bonded with the substrate, while the bridges typically remain weakly bonded with the substrate. As a result, the functional components on the islands (e.g., Figure 3a) are usually mechanically isolated, since the applied strains are mostly accommodated by the stretchable interconnects, due to their much higher deformability. The focus of the island-bridge designs is typically on the structural interconnects, such as the arc-shaped, serpentine, 2D spiral, and 3D helical forms, as we elaborated below.

2.2.1. Arc-Shaped Interconnects

Similar to the wavy structure formed with a selective bonding, the arc-shaped interconnects are transformed from a planar configuration through compressive buckling. Figure 3a illustrates schematically the fabrication process and mechanics model for a representative island mesh with arc-shaped interconnects.^[115] Under stretching, arc-shaped interconnects can effectively deform out of plane to accommodate the applied strain. Due to the much lower stiffness of the interconnects compared to the islands, such designs provide an effective mechanical isolation of the islands. Figure 3b presents an SEM image of a stretchable silicon mesh along with theoretical results for the strain distribution in a silicon island element,

selectively bonded onto the substrate. Adapted with permission.^[45] Copyright 2006, Wiley-VCH. d) SEM images of the 1D and 2D wavy ribbons fully bonded onto PDMS substrate. Left image, reproduced with permission.^[103] Copyright 2007, National Academy of Sciences. Right image, reproduced with permission.^[104] Copyright 2007, American Chemical Society. e) SEM image of ribbons with selectively bonding on PDMS substrate. Reproduced with permission.^[105] Copyright 2006, Nature Publishing Group. f) Wavy configuration with fully bonded strategy. Top panels are the schematic illustration of the process for fabricating wavy structure on PDMS substrates. Left bottom panel is the wavelength and the amplitude as a function of prestrain. Right bottom panel is the wavelength and the amplitude as a function of applied strain. Reproduced with permission.^[103] Copyright 2007, National Academy of Sciences. g) Wavy configuration with selectively bonded strategy. Top panels are the schematic illustration of fabricating precisely controlled wavy structure on PDMS substrates. Bottom left panel is GaAs ribbon structures formed on PDMS substrates with different prestrains. Bottom right panel is the GaAs ribbon structures with different width of inactivated region W_{in} . Top panels, reproduced with permission.^[112] Copyright 2007, Elsevier. Bottom panel, reproduced with permission.^[105] Copyright 2006, Nature Publishing Group. h) Optical images of a wavy structure of stretchable single crystal Si p–n diode with different strains applied (–11% (top), 0% (middle), and 11% (bottom)). Reproduced with permission.^[102] Copyright 2006, American Association for the Advancement of Science. i) Optical images of the biaxial stretchable integrated circuits. Reproduced with permission.^[114] Copyright 2008, American Association for the Advancement of Science. j) SEM image of field-effect transistors based on controlled buckled GaAs thin films. Reproduced with permission.^[45] Copyright 2006, Wiley-VCH.

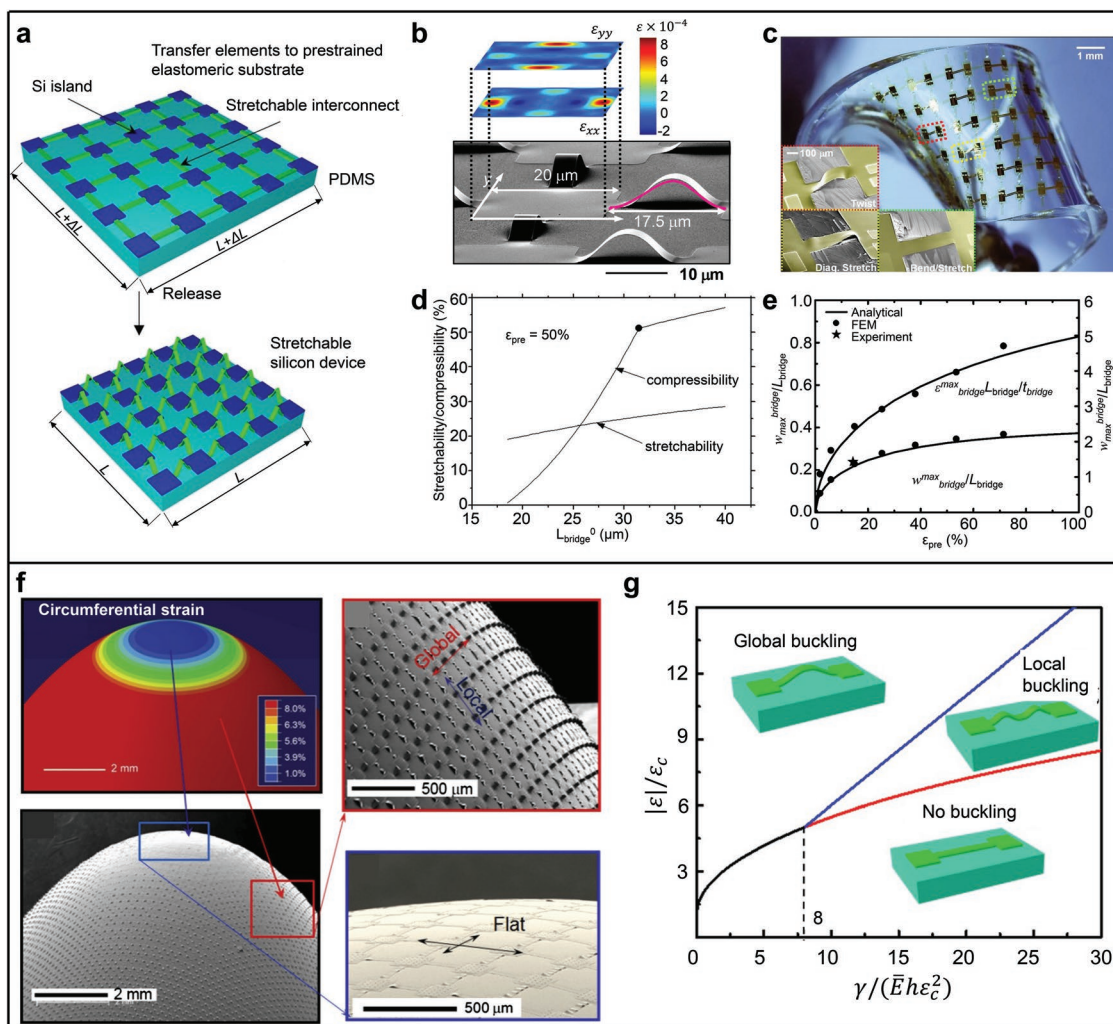


Figure 3. Arc-Shaped designs. a) Schematic illustration of the fabrication and mechanics model of the device island mesh with arc-shaped design. Reproduced with permission.^[115] Copyright 2009, American Institute of Physics. b) SEM image of a stretchable silicon mesh with the theoretical results of the strain distribution in an island element. Reproduced with permission.^[26] Copyright 2008, Nature Publishing Group. c) Optical images of stretchable CMOS inverter arrays, presenting the representative deformations: diagonal stretching, twisting, and bending. The insets are SEM images for each case. Reproduced with permission.^[41] Copyright 2008, National Academy of Sciences. d) Stretchability and compressibility as a function of the length of arc-shaped bridge for the noncoplanar mesh design. Reproduced with permission.^[115] Copyright 2009, American Institute of Physics. e) Normalized maximum deflection and maximum strain of the arc-shaped bridge versus the prestrain of the substrate. Reproduced with permission.^[116] Copyright 2013, Royal Society of Chemistry. f) Distribution of circumferential strain for a parabolic elastomeric substrate given by the mechanics model, and the SEM images of buckling patterns of interconnects. Reproduced with permission.^[118] Copyright 2010, Royal Society of Chemistry. g) Normalized compressive strain versus normalized work of adhesion to distinguish different buckling modes. Reproduced with permission.^[119] Copyright 2017, ASME.

where the maximum strain is only 0.08%, much smaller than the failure strain ($\approx 2\%$) of silicon. These thin, narrow arched bridge structures can also undergo other complex deformations, such as the twisting, shearing, and bending, with an example shown in Figure 3c.

Theoretical models can be built to serve as a design basis of such arc-shaped interconnects. For example, Song et al.^[115] developed a mechanics model to study the buckling deformations, by modeling the structure as a clamped beam. The out-of-plane displacement of the interconnect was assumed to take a sinusoidal form, where the amplitude can be determined from minimization of the total strain energy. Based on this model, the relation of between the stretchability and compressibility

of the system and the initial bridge length can be predicted, as shown in Figure 3d for the case with the prestrain 50%. Both the stretchability and compressibility increase with the length of interconnects, while the compressibility increases much faster than the stretchability. This model is primarily applicable to the case where the out-of-plane displacement of the interconnect is relatively small compared to the bridge length, because the assumption of the sinusoidal postbuckling configuration is not sufficiently accurate in the case of large out-of-plane displacements. To address this limitation, a finite deformation model was developed,^[116] without the use of the sinusoidal assumption of interconnect buckling deformation. This model provides an accurate solution to the deflection and peak strain

in the interconnects, as shown in Figure 3e. These results show that thin and long interconnects are preferred to increase the stretchability.

Arc-shaped bridge designs can conform to the surfaces of soft bio-tissues, such as the epidermis, the epicardium, and the brain, to provide portable healthcare functionalities. When the electronic circuit mesh is mapped onto these complex, curvilinear, 3D shape, the arc-shaped bridges could experience various different deformation modes (e.g., global buckling, local buckling, and no buckling), depending on the local strain and the strength of the interfacial adhesion,^[117,118] as shown in Figure 3f. In the case of a weak adhesion with $\gamma \leq 8Eh\epsilon_c^2$ (with E and h being the Young's modulus and the thickness of bridge), the local buckling mode never occurs, and the conditions to induce the global buckling and no buckling are given by

$$\text{For } \gamma \leq 8Eh\epsilon_c^2, \begin{cases} \text{no buckling} & \text{if } |\epsilon| < \epsilon_c + \sqrt{\frac{2\gamma}{Eh}} \\ \text{global buckling} & \text{if } |\epsilon| \geq \epsilon_c + \sqrt{\frac{2\gamma}{Eh}} \end{cases} \quad (5)$$

In the case of a relatively strong adhesion with $\gamma > 8Eh\epsilon_c^2$, the different buckling modes are controlled by

$$\text{For } \gamma > 8Eh\epsilon_c^2, \begin{cases} \text{no buckling} & \text{if } |\epsilon| < 5\left(\frac{\gamma\sqrt{\epsilon_c}}{Eh}\right)^{2/5} \\ \text{local buckling} & \text{if } 5\left(\frac{\gamma\sqrt{\epsilon_c}}{Eh}\right)^{2/5} \leq |\epsilon| < \epsilon_c + \frac{\gamma}{2Eh\epsilon_c} \\ \text{global buckling} & \text{if } \epsilon_c + \frac{\gamma}{2Eh\epsilon_c} < |\epsilon| \end{cases} \quad (6)$$

The above relations distinguish the different buckling modes and are plotted in Figure 3g.^[119] The results agree well with the experimental observations in Figure 3f. Therefore, these theoretical findings provide a useful reference to predict the buckling modes of arc-shaped interconnects over an arbitrary surface.

2.2.2. Serpentine Interconnects

Figure 4a shows a 3D schematic illustration of the serpentine unit cell that consists of two curved sections (i.e., the *arc*) and three linear sections (i.e., the *arm*).^[120,121] The in-plane geometry of the unit cell can be defined by four independent geometric parameters, including the arc radius R , the width w , the arm length l , and the arc opening angle α . Moreover, these parameters can be normalized as $w/R, l/R$, and α , corresponding to the three degrees of freedom in the 3D design space, as shown in the bottom panel of Figure 4a. Different combinations of the three normalized parameters can be represented as points in the first and the fifth quadrants of this 3D design space to define the in-plane serpentine geometries, demonstrating the diversity of the serpentine designs to meet different requirements.^[122–127]

In practical applications, the serpentine interconnects can be either suspended (or nonbonding without considering the constraints from the substrate during deformations) or fully

bonded to the substrate. Their mechanical behaviors are different in these conditions, and must to be discussed separately.

For the suspended serpentine interconnects, Zhang et al.^[128] developed analytical models to thoroughly study the buckling physics in serpentine structures, providing a design approach of the serpentine interconnects to achieve a desired stretchability. By analyzing the effect of serpentine geometric parameters, e.g., the thickness t , the spacing l_1 and the width w (Figure 4b), the critical buckling strain was found to be proportional to the square of the aspect ratio (t^2/w^2), and can be given by

$$\epsilon_c = \frac{a(a^2 + 6) + \frac{3\pi}{4}(2a^2 + 1) - \frac{9(a^2 + \pi a + 1)^2}{8a + \pi + 8(2a + \pi)m^2}}{f_1(m) + f_2(m)a + f_3(m)a^2} \sqrt{\frac{G}{E}} \frac{t^2}{w^2} \quad (7)$$

where G and E are the shear modulus and Young's modulus of the interconnect material, respectively; $a = l_2/l_1$ is the length/spacing ratio; and f_1, f_2 , and f_3 describe the contributions of each second-order term of length scale to the lateral buckling, which depend only on the unit cell number (m) of the serpentine interconnect.

When the applied strain $\epsilon_{\text{applied}} < \epsilon_c$, the serpentine interconnect does not undergo buckling, and the normalized elastic stretchability $\epsilon_{\text{elastic-stretchability}} w / (\epsilon_{\text{yield}} l_1)$ can be given as

$$\frac{\epsilon_{\text{elastic-stretchability}} w}{\epsilon_{\text{yield}} l_1} = \frac{4\eta^3 + 6(\pi - 2)\eta^2 - 12(\pi - 3)\eta + 9\pi - 28}{12\eta} \quad (8)$$

where ϵ_{yield} is the yield strain of serpentine material, and $\eta = h/l_1$ is the height/spacing ratio. Equation (8) shows that the normalized elastic stretchability increases with increasing height/spacing ratio η and unit cell number m , as shown in Figure 4c. As the critical strain ϵ_c scales with t^2/w^2 , the above Equation (8) of nonbuckled serpentine interconnects holds mainly for relative thick interconnects.

When the applied strain $\epsilon_{\text{applied}} > \epsilon_c$, the serpentine interconnect undergoes lateral buckling. In this case, the out-of-plane and in-plane bending strains during the postbuckling processes are proportional to the normalized thickness and width, respectively. As such, the maximum principal strain in the regime of reversible deformations can be written as

$$\epsilon_{\text{max}} = g_1(m, a) \sqrt{\epsilon_{\text{applied}}} \frac{t}{l_1} + g_2(m, a) \epsilon_{\text{applied}}^2 \frac{w}{l_1} \quad (9)$$

where the first and second terms on the right-hand side correspond to the out-of-plane and in-plane bending strains, respectively; g_1 and g_2 are the coefficients of proportionality, depending on the number of unit cell m and the length/spacing ratio a ; and $\epsilon_{\text{applied}}$ is the applied strain. Equation (9) indicates that at small applied strains ($\sqrt{\epsilon_{\text{applied}}} \gg \epsilon_{\text{applied}}^2$), the out-of-plane bending strain dominates in the initial stage of postbuckling. As the applied strain increase until $\sqrt{\epsilon_{\text{applied}}} - \epsilon_{\text{applied}}^2$, the in-plane bending strain begins to play an important role.

Based on the yield criterion of $\epsilon_{\text{max}} = \epsilon_{\text{yield}}$, where ϵ_{yield} is the yield strain of the interconnect material, the elastic stretchability of the serpentine can be given as

$$\epsilon_{\text{elastic-stretchability}} = \lambda^2 \quad (10)$$

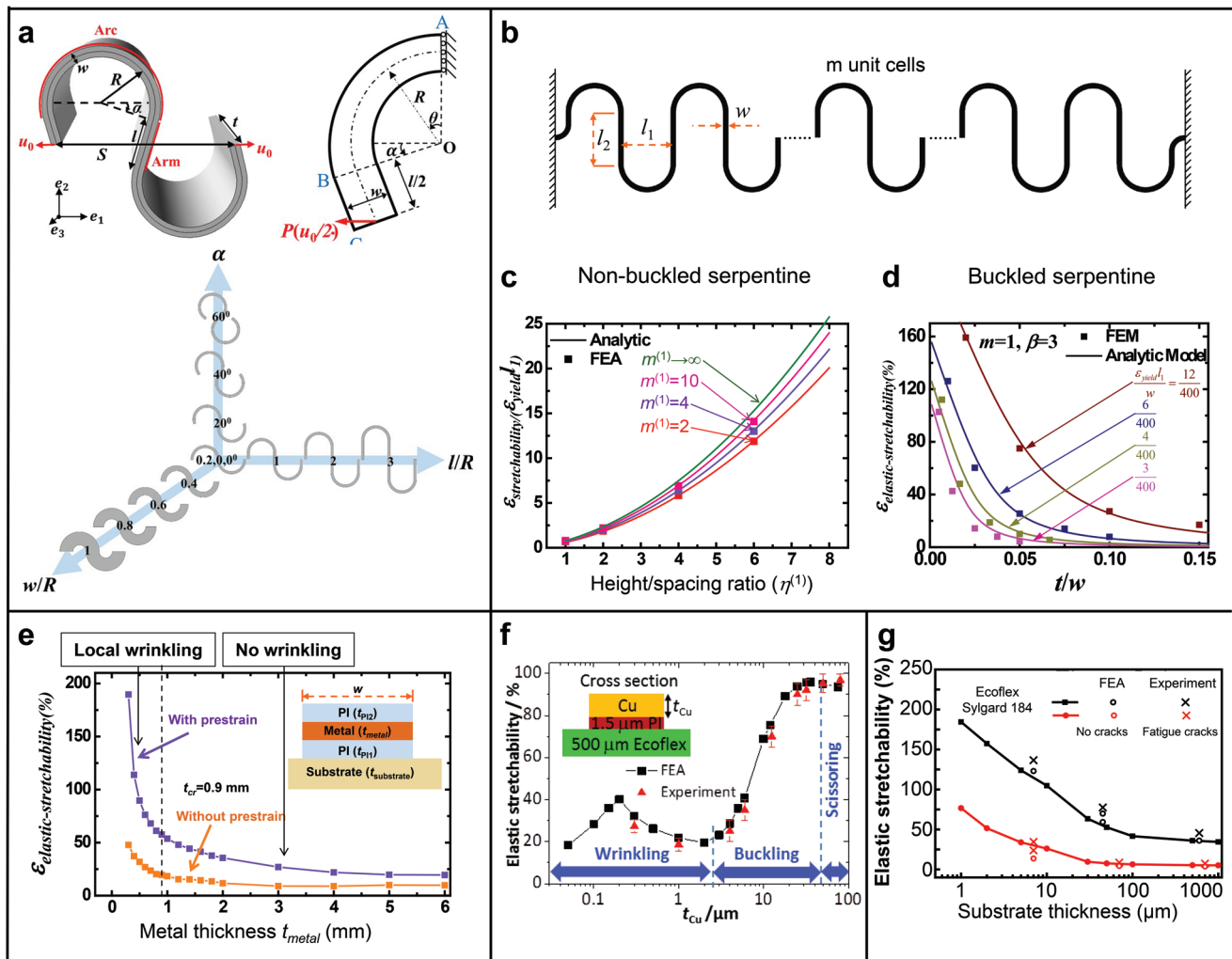


Figure 4. Serpentine interconnects designs. a) Top panels are the schematic illustration of a 3D serpentine unit cell and 2D boundary conditions labeled. Bottom panel is the 3D design space for serpentine shapes defined by three dimensionless geometric parameters. Reproduced with permission.^[120] Copyright 2017, ASME. b) Schematic illustration of geometric parameters for a representative serpentine interconnect with m unit cells. Reproduced with permission.^[128] Copyright 2013, The Royal Society of Chemistry. c) Normalized elastic stretchability of nonbuckled serpentine interconnects as a function of height/spacing ratio for different number of unit cells. Reproduced with permission.^[147] Copyright 2013, Elsevier. d) Elastic stretchability of buckled serpentine interconnects as a function of thickness/width ratio. Reproduced with permission.^[128] Copyright 2013, The Royal Society of Chemistry. e) The prestrain strategy for increasing stretchability of fully bonded serpentine interconnects. Influence of geometric parameters for metal thickness on the elastic stretchability of serpentine interconnects with and without prestrain. Reproduced with permission.^[129] Copyright 2013, Wiley-VCH. f) Experiment and FEA results about the relation of deformation and elastic stretchability of serpentine interconnects with the thickness of Cu interconnects. Three regimes of deformation occurred: wrinkling, buckling, and scissoring. Reproduced with permission.^[130] Copyright 2016, Wiley-VCH. g) FEA and experimental results of the influence of the substrate thickness and substrate modulus on the stretchability of serpentine interconnects. Reproduced with permission.^[131] Copyright 2017, Wiley-VCH.

where $\lambda > 0$ is the solution to the following fourth order algebraic equation which has a single positive solution

$$g_2(m, a)\lambda^4 + g_1(m, a)\frac{t}{w}\lambda - \frac{\epsilon_{\text{yield}}l_1}{w} = 0 \quad (11)$$

Equations (10) and (11) show that the elastic stretchability only depends on four dimensionless parameters, t/w , $\epsilon_{\text{yield}}l_1/w$, m , and β , as demonstrated in Figure 4d, where the elastic stretchability increases with decreasing t/w , or increasing $\epsilon_{\text{yield}}l_1/w/m$ and a .

Considering the degree of integration of the system in practical applications, the spacing of functional device islands (i.e., the physical space for serpentine interconnects) is often limited. This situation typically demands a large number of unit cells to achieve large length/spacing ratios a (and thus large stretchability), in layouts that maintain a relatively small amplitude.

For fully bonded serpentine interconnects, mechanical deformations become more complex than the suspended serpentine structure, due to the constraints from the solid substrate. During stretching, the substrate can confine the unraveling of serpentine interconnects, thereby decreasing the

stretchability. Zhang et al.^[129] proposed a prestrain strategy, in which serpentine interconnects fully bonded to a prestretched substrate can yield significantly improved mechanics, with the stretchability increased by more than two times compared to the case without prestrain (Figure 4e). Through experiments and finite element analysis (FEA), two different buckling modes of serpentine interconnects at different metal thicknesses, namely local wrinkling and wrinkle-free, are revealed. The analytical model based on this mechanism can predict the buckling wavelength at different metal thicknesses, as shown in Figure 4e. Note that this prestrain strategy can be applied not only to the serpentine interconnects, but also to other interconnect layouts, e.g., the horseshoe, fractal, and 3D helical patterns.

Moreover, Su et al.^[130] presented a combined theoretical and experimental study of the elastic stretchability of serpentine interconnects in a very wide range of interconnect thicknesses, where the deformation mechanisms involve wrinkling, buckling, and scissoring, with the increasing thickness (Figure 4f). Pan et al.^[131] investigated the influence of the substrate thickness and substrate modulus on the stretchability of serpentine interconnects, showing an enhancement of the elastic stretchability through the reduction of the substrate thickness (Figure 4g).

2.2.3. 2D Spiral Interconnects

2D spiral shapes are curves formed by winding a circle from the fixed point. Such geometries are very common in nature, such as the famous golden spiral and nautilus shell with approximately golden spiral structure (Figure 5a). When a lateral force is applied to this 2D spiral-shaped structure, the spiral unwinds through out-of-plane deformations to accommodate the strain energy. Once the force is removed, this strain energy is released, returning the spiral to its original shape and position. The 2D spiral-inspired bridge/interconnect design could create strain-free connected islands, with larger levels of stretchability compared to those of conventional serpentine interconnects, given the same area coverage and contour length.

For a stretchable interconnect, a uniform and small curvature usually contributes to a large stretchability.^[132] On this basis, the Archimedean spiral ($r = \pm a\theta^t$, $t < 1$ in a polar coordinate system) with uniform and small curvature is a better choice than golden spiral.^[133,134] Lv et al.^[132] studied the stretchability of Archimedean spiral interconnects by FEA. Figure 5b shows up to 200% stretchability of Archimedean spiral structure and its deformed states under 80% and 200% strains, where in-plane stretching induces both twisting and bending deformations of the interconnect (also displayed in the graph of Figure 5c). Note that the unwinding deformation compensates for the in-plane stretching. Upon release of a large applied strain, even if plastic deformations occur (e.g., 200% strain released in Figure 5b), the interconnection returns almost completely to the undeformed shape. Regions that enter the plastic zone can be quite limited ($\approx 1\%$, as shown in the graph of Figure 5c), such that most of the interconnects remain in the elastic domain.

To make the spiral-based structure to fit into the nonsquare areas, a modified Archimedean spiral can be used, as shown in the top panel of Figure 5d. The key is to modify the original

Archimedean spiral $r = \pm a\theta^t$, $t < 1$ by multiplying with a smooth approximation to a step function of θ and then inserting straight lines to fit the in-plane area. The FEA results in the bottom panel of Figure 5d show that the modified Archimedes spiral becomes more stretchable, with $>250\%$ elastic stretchability and 325% stretchability before fracture. The addition of the straight part enhances the ability of the structure to deform out-of-plane, without introducing large curvatures. Figure 5e presents an SEM image of Archimedes spiral as an electroplated copper interconnect, suspended on the silicon substrate.^[135]

As an alternative to the Archimedes spiral, a 2D spiral-node design was proposed to limit the out-of-plane deformations during the unwinding process,^[136] as illustrated in Figure 5f. This 2D spiral structure fabricated by conventional microfabrication techniques is configured as $1.6\ \mu\text{m}$ thin spiral ribbons of silicon wrapped around each circular silicon island (i.e., node; $200\ \mu\text{m}$ in diameter). The active devices are placed on each island and connected mechanically and electrically via two 2D spiral interconnects to the devices on neighboring islands in a 2D network. Based on this design, all of the applied strain during the expansion process is accommodated by the spiral ribbons, while the active device area can remain almost strain-free. The maximum principal strain in the spiral arm, $\epsilon_{\text{max}} = w/2R$, is encountered in the section that unrolls last, where w is the thickness of the spiral ribbon and R is the radius of the innermost spiral winding. The force–displacement relationship based on FEA is shown in Figure 5g, where the unwinding of the spirals causes a gradual increase in force until the end-point is reached. A maximum strain of $\epsilon_{\text{max}} = 2\%$ occurs for a displacement of $6.36\ \text{mm}$, which translates to a stretchability of $>3000\%$, noting that the initial diameter of the circular silicon island is $200\ \mu\text{m}$. Rojas et al.^[137] analyzed the design parameters of 2D spiral-node, and proposed an area efficient design based on a network of hexagonal islands. The FEA indicates that large strains appear at the two ends of arms, and that by introducing the serpentine structures (Figure 5h), the force required to achieve the displacement is halved (e.g., from $60\ \mu\text{N}$ for a straight arm to $30\ \mu\text{N}$ for the one with the serpentine structure). In addition, the strain is also halved and distributed more evenly along the arm, rather than being concentrated at a single point.

Rehman et al.^[138] further optimized the 2D spiral interconnect design by incorporating serpentine structures, as shown in the bottom left panel of Figure 5i, to improve the stretchability. Compared to the original spiral structure, as shown in the top left panel of Figure 5i, the optimized structure replaces the original curved arm with semicircular serpentine arm structures and horseshoe structures. As displayed by the stress analyses in the right panel of Figure 5i, the maximum stress of this optimized compound spiral is reduced to $1779\ \text{MPa}$, corresponding to a 58.47% reduction, in comparison to the original spiral structure.

2.2.4. 3D Helical Interconnects

The 3D helical interconnects offer structural design with exceptionally low effective modulus and high elastic stretchability, as a particularly very attractive design in stretchable inorganic

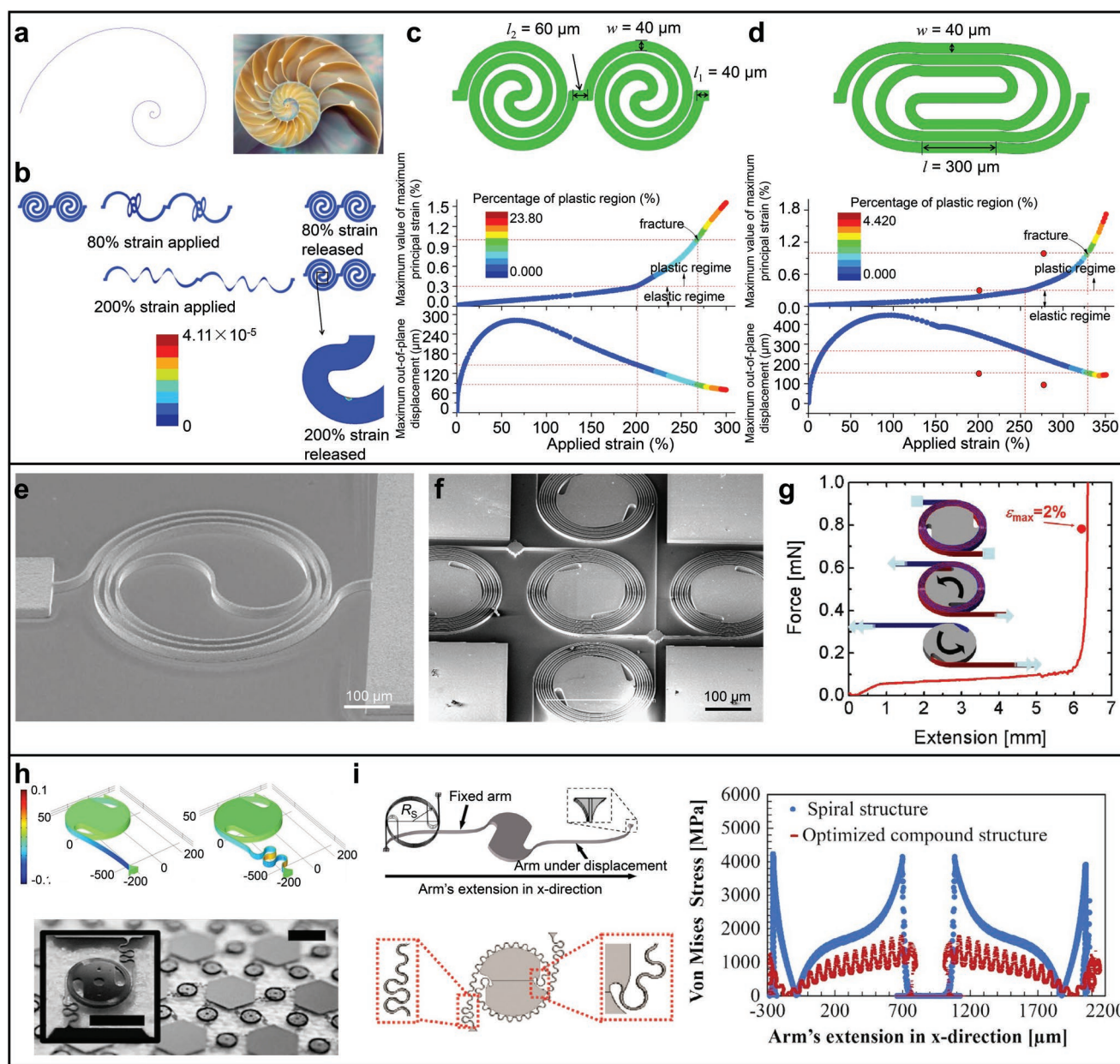


Figure 5. 2D spiral interconnects designs. a) The golden spiral and nautilus shell with approximately golden spiral structure. b) Deformed and undeformed shapes of an Archimedean spiral structure. Geometry and FEA results for an original (c) and modified (d) Archimedean spiral design. Bottom panel: the relation between the maximum principal strain, maximum out-of-plane displacement and the applied strain, indicating the percentage of plastic zone for the original and modified Archimedean spiral design. The red dots in (d) show the corresponding results for the original spiral design. Here, the stretchability is defined as the critical strain where maximum principal strain exceeds the fracture strain, 1%. Reproduced with permission.^[132] Copyright 2014, Elsevier. e) SEM image of Archimedes spiral electroplated Cu interconnect. Reproduced with permission.^[135] Copyright 2016, IOP Publishing. f) SEM image of 2D spiral-node design. g) FEA result of the relation of the force and displacement of a single Si islands with two spirals. Reproduced with permission.^[136] Copyright 2007, IEEE. h) Top panels are FEA results of strain distribution along spring structures without (left top) and with (right top) serpentine ending. Bottom panels are the photograph and zoom-in of an array of 2D spirals with serpentine ending (scale bar is 1 mm, 0.5 mm for the zoom-in). Reproduced with permission.^[137] Copyright 2014, American Institute of Physics. i) Schematics of 2D spiral structure (left top) and optimized compound structure (left bottom), and stress distribution comparison between original spiral and compound structure along their arms (right). Adapted with permission.^[138] Copyright 2017, Elsevier.

electronics. Unlike 2D serpentine interconnects which involve sharp strain concentrations upon stretching deformation, the 3D helical layouts involve only minor physical coupling to the substrate, and therefore, can effectively suppress these

strain concentrations through more uniform 3D spatial deformations.

Figure 6a highlights the procedures for the forming helical structures by this type of deterministic compressive buckling

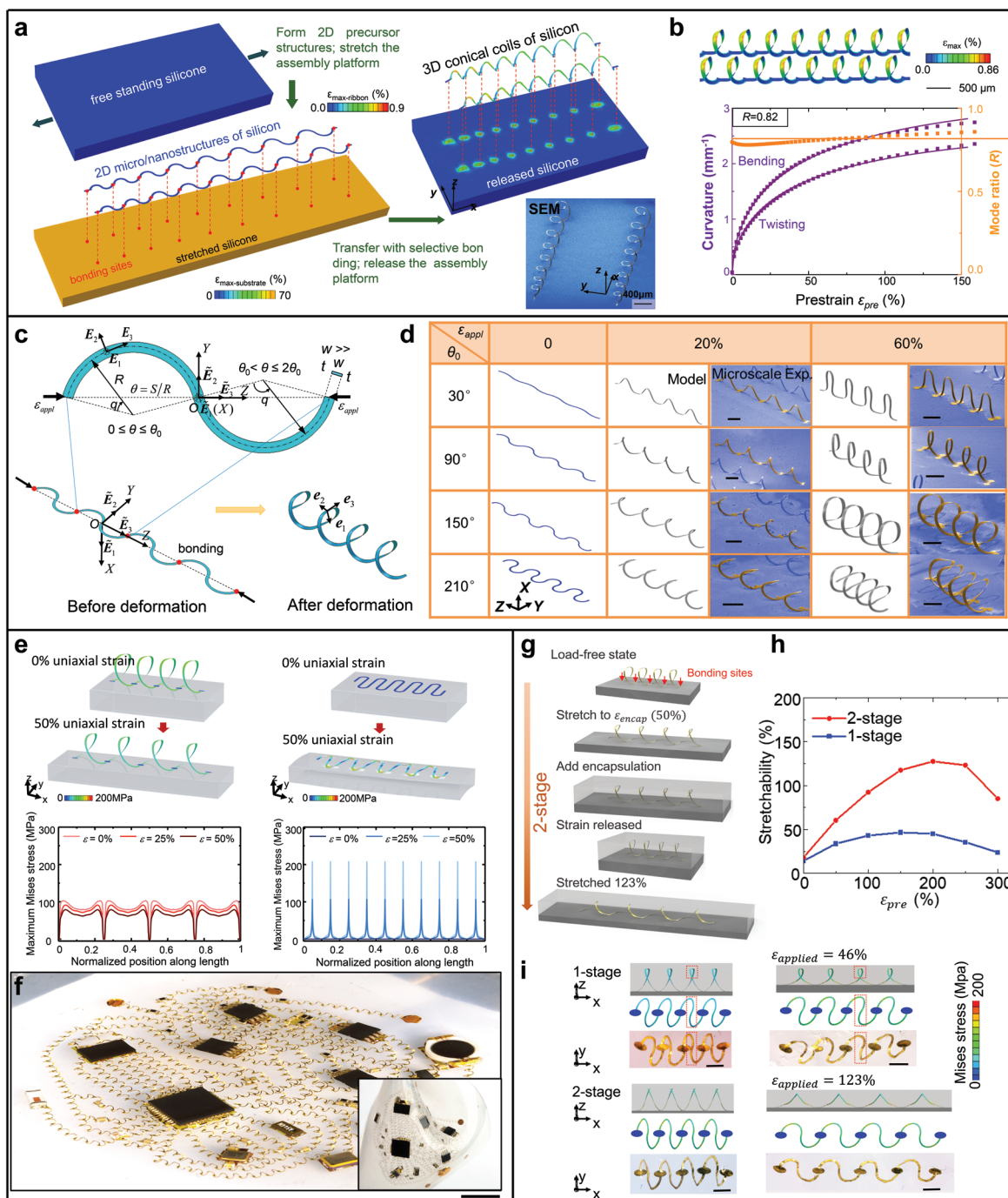


Figure 6. 3D helical interconnects designs. a) Schematic illustration of the assembly procedures for the 3D helical interconnects formed by the deterministic compressive buckling. 2D serpentine interconnect bonded at selected sites (red dots) onto a prestretched silicone elastomer. The SEM image at bottom shows the experimental result. b) The maximum principal strain in 3D helical interconnect (top). Bottom: The relationship of the average curvature components and mode ratio of a 3D helical interconnect on the prestrain. Adapted with permission.^[139] Copyright 2015, American Association for the Advancement of Science. c) Schematic of the mechanics model of the buckling-guided 3D helical interconnects both in the undeformed and deformed states. The black dots denote the strong bonding sites with the substrate. A typical serpentine unit cell consists of two identical arcs, each with the same radius R and arc angle θ_0 . d) Model predictions and microscale experimental images of the deformed configurations of 3D helical with various arc angle at different levels of applied strain. Adapted with permission.^[141] Copyright 2016, Wiley-VCH. e) Stress distribution in 2D serpentine and 3D helical interconnects. f) Optical image of a skin-mounted device for health monitoring with 3D helical interconnects at a state of 50% bi-axially stretching. Inset is the optical image of the device. Reproduced with permission.^[142] Copyright 2017, Nature Publishing Group. g) Schematic illustration of two-stage encapsulation strategies for 3D helical interconnects. h) Comparison of elastic stretchability between one-stage and two-stage encapsulation for 3D helical interconnects formed with different prestrains. i) Optical images and FEA results on the undeformed and deformed configurations of 3D helical interconnects with one-stage and two-stage encapsulation strategies. Scale bars are 1 mm. Adapted with permission.^[146] Copyright 2019, Wiley-VCH.

process. Filamentary serpentine traces with predefined bonding sites serve as the 2D precursors that are transferred onto a prestretched elastomer substrate, with sites of strong bonding at red dots in Figure 6a. When the prestrain in the substrate is released, the 2D serpentine precursor is subjected to compressive stresses, triggering the simultaneous in-plane and out-of-plane translational/rotational motions and bending/twisting deformations in the nonbonded regions, which results in the formation of a 3D helical structure. Figure 6b shows the dependence of the average curvature components and mode ratio of a 3D helical interconnect on the prestrain. The maximum principal strain induced by the assembly process is distributed quite uniformly along the structure (top panel of Figure 6b), which enables an exceptionally large stretchability and mechanical robustness.^[139,140]

Based on an energetic approach that takes into account the various forms of spatially dependent deformations, an analytic model of the compressive buckling in serpentine interconnects was developed to predict the deformed configurations and maximum strains of 3D helical interconnects.^[141] Figure 6c illustrates the key geometric parameters associated with the mechanics model, considering both the undeformed and deformed configurations, where the red dots denote the sites of strong bonding with the elastomer substrate. Figure 6d shows the model predictions and microscale experimental results of the deformed configurations at different levels of applied strain (20% and 60%) for a wide range of serpentine geometries (arc angle θ from 30° to 210°).^[141] The model predictions agree well with experimental results in all of the different cases, suggesting that the analytic model can be used as a theoretical reference of design optimization in practical applications.

A comparison of the stress distributions in the 2D serpentine and 3D helical interconnects (Figure 6e) shows that the Mises stresses in the 3D layouts vary smoothly and uniformly under uniaxial stretching, while the deformations of the 2D serpentine interconnect lead to sharp, unavoidable stress concentrations at the arc regions.^[142] As a result, the 3D helical interconnects offer a higher stretchability than the 2D serpentine interconnects, in a manner that avoids propensity for localized crack formation or fracture. Figure 6f demonstrates a representative application of 3D helical interconnects in wearable health monitors,^[142] capable of continuous, wireless monitoring of electrophysiological signals from the mounted locations on the skin. The overall layout ensures a uniform and extreme stretchability and bendability in any direction, and meanwhile minimizes the overall system size (≈ 30 mm in this case, which consists of ≈ 250 3D helices, ≈ 500 bonding sites, and ≈ 50 component chips).^[142]

In practical applications, direct physical contact with objects in the environment could cause an unencapsulated device to fail, due to physical or chemical damage.^[143–145] Furthermore, mechanical isolation of the rigid part of the device from human tissue could be important in many cases.^[77] Therefore, the development of a reliable encapsulation approach to protect and isolate the inorganic electronic devices is critically important. The conventional method for encapsulation, referred to as the “one-stage encapsulation” strategy, involves the direct solidification of a soft encapsulation material delivered in the form of liquid prepolymer to the device in its unstretched, load-free configuration. The constraints of the solid encapsulant on

the interconnect deformations can, however, greatly limit the stretchability. To overcome this limitation, Li et al.^[146] developed a generic, “two-stage encapsulation” strategy, which forms the encapsulation while the system is in a prestrained state (encapsulating strain $\varepsilon_{\text{encap}}$), and then releasing the prestretch to complete this two-stage process (Figure 6g,h). This strategy can significantly reduce the constraints of solid encapsulation on the interconnect deformations and maximize the stretchability. Meanwhile, this strategy can be widely applicable to various interconnect configurations, e.g., serpentine, fractal, and 3D helical interconnects.

The key mechanisms underlying the improvements that result from the two-stage encapsulation strategy can be attributed to the 3D configuration of the interconnects and the unique deformation modes. For a 3D helical interconnects formed by a relative large compressive strain, knot-like structures form in the as-assembled state, which mainly results from in-plane rotational motions at the peaks of the 3D helices (Figure 6i). These knot-like structures are difficult to unravel under stretching, which limits the stretchability of 3D helical interconnects encapsulated by the one-stage strategy. With two-stage encapsulation, these knot-like structures can be unwound in advance by applying the encapsulation strain. After the encapsulation material is cast, the encapsulation material imposes a constraint on the interconnect that avoids the recovery of the knot-like structures, thereby improving the stretchability (Figure 6h).

2.3. Fractal-Inspired Designs

Fractal-inspired design concepts provide a powerful approach to simultaneously achieve large stretchability and high areal coverage in stretchable inorganic electronics. These concepts can be exploited in both the designs of stretchable interconnects and functional device components, as discussed separately in this section.

The fractal inspired interconnect designs provide a straightforward and systematic set of rules for filling a 2D space with curved filamentary structures to a level determined by the fractal order. Figure 7a provides an example of a fractal layout that introduces the serpentine configuration as the first order structure, and forms the second, third, and fourth order structures, according to the self-similar geometry. As with the serpentine interconnects, the fractal inspired interconnects can also be fully bonded, or nonbonded to the elastomer substrate. For a nonbonded/suspended interconnect stretched from two ends, nonbuckled in-plane deformations occur for large t/w (typically ≥ 1), and buckled spatial deformations for small t/w (usually $\leq 1/5$).

For the nonbuckled in-plane deformations, Zhang et al.^[147] developed analytical models of flexibility and elastic stretchability by establishing recursive formulae at different fractal orders. The analytic solution of the elastic stretchability agrees well with FEA results, as illustrated in Figure 7b. In particular, the normalized stretchability, $\varepsilon_{\text{stretchability}} w / [\varepsilon_{\text{yield}}^{(n)}]$, increases with fractal order (n), and is more than doubled for each n increasing by 1, suggesting that the high-order fractal designs can greatly improve the elastic limits of the interconnects.

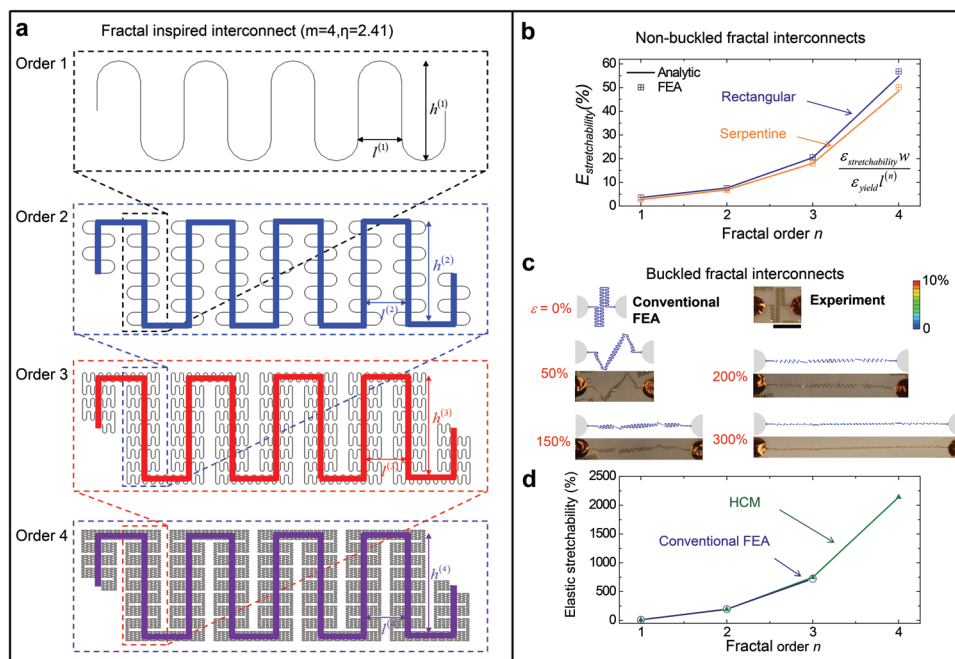


Figure 7. Principals for fractal-inspired interconnects designs. a) Schematic illustration of fractal layout from order 1 to 4. b) The normalized stretchability as a function of the fractal orders. Adapted with permission.^[147] Copyright 2013, Elsevier. c) Top: Optical images and corresponding FEA results of the ordered unraveling mechanism of a fractal serpentine interconnect. Reproduced with permission.^[148] Copyright 2013, Nature Publishing Group. d) FEA and HCM results of the elastic stretchability at various fractal interconnects (from order 1 to 4). Adapted with permission.^[149] Copyright 2014, Elsevier.

For buckled spatial deformations, Xu et al.^[148] demonstrated an interesting deformation mechanism of ordered unraveling, as shown in the top panel of Figure 7c. Both the FEA and experimental results illustrate that the second-order and first-order structures unravel sequentially, in which the second-order structure unravels first, while the first-order structures remain substantially undeformed. Unraveling of the first-order structures starts only after the second-order structures have been fully extended (e.g., the applied strain of $\approx 150\%$ in Figure 7c), and this unraveling process continues until the maximum stretchability ($\approx 300\%$) is reached. Based on this mechanism of ordered unraveling during the postbuckling deformations, Zhang et al.^[149] developed an effective hierarchical computational model (HCM), that provides a high predictive accuracy, as validated by experiments and FEA, while significantly reducing the computational effort and cost. The results in the bottom panel of Figure 7c illustrate that the elastic stretchability can be increased by ≈ 200 times, with the fractal order increasing from 1 to 4, clearly showing the advantages of fractal-inspired designs. It is important to note that in this case, the elastic stretchability is the stretchability of the fractal interconnect rather than that of system, since the system-level stretchability also depends on the ratio of the length to spacing of the island. For example, when this ratio is 20:1 (corresponding to $\approx 90\%$ areal coverage of the island), 1000% interconnect-level stretchability only translates to $\approx 50\%$ system-level stretchability.

Beyond the specific fractal rectangular/serpentine interconnects discussed above, fractal design concepts can be applied to other basic interconnect configurations, e.g., the zigzag, sinusoidal, serpentine and horseshoe shapes,^[150,151] for an additional level of design flexibility.

For stretchable functional components, fractal layouts not only improve the stretchability while increasing the space filling ratio, but also allow conformal matching to soft materials and curvilinear surfaces, which is very important for applications in bioelectronics and other areas in bio-interfaces and bio-inspired designs.^[152–156] The top panel of Figure 8a presents six representative fractal-inspired layouts,^[154] ranging from lines (Koch, Peano, Hilbert) to loops (Moore, Vicsek) and branch-like meshes (Greek cross), which can be applied to the design of electrophysiological sensors, precision monitors/actuators, and radio frequency antennas. Fan et al.^[154] studied the deformations of various fractal layouts by high precision electromechanical measurements and 3D FEA, showing a high degree of agreement between FEA predictions and experimental results (Figure 8a, middle and bottom). The table in the top panel of Figure 8b summarizes the calculated x - and y -directional stretchabilities of five different second-order Peano layouts of metal wires mounted onto an elastomer. Because of their isotropic stretchability, the “Half-and-Half” layouts are well suited for device design that demands high stretchabilities along various different directions, for example, in epidermal electronics. As demonstrated in the bottom panels of Figure 8b, the third-order Peano layout of metal wires conformally contacts with the skin.^[154] Moreover, fractal-inspired electrodes that offer large area coverage, high filling fraction, and conformal contact to curved surfaces can be utilized in cardiac electrotherapy to deliver electrical stimulation and to cardiac electrical activity.^[152] As shown in Figure 8c, a fractal electrode array distributed over a rabbit heart circumference can provide direct interfaces to deliver spatially and

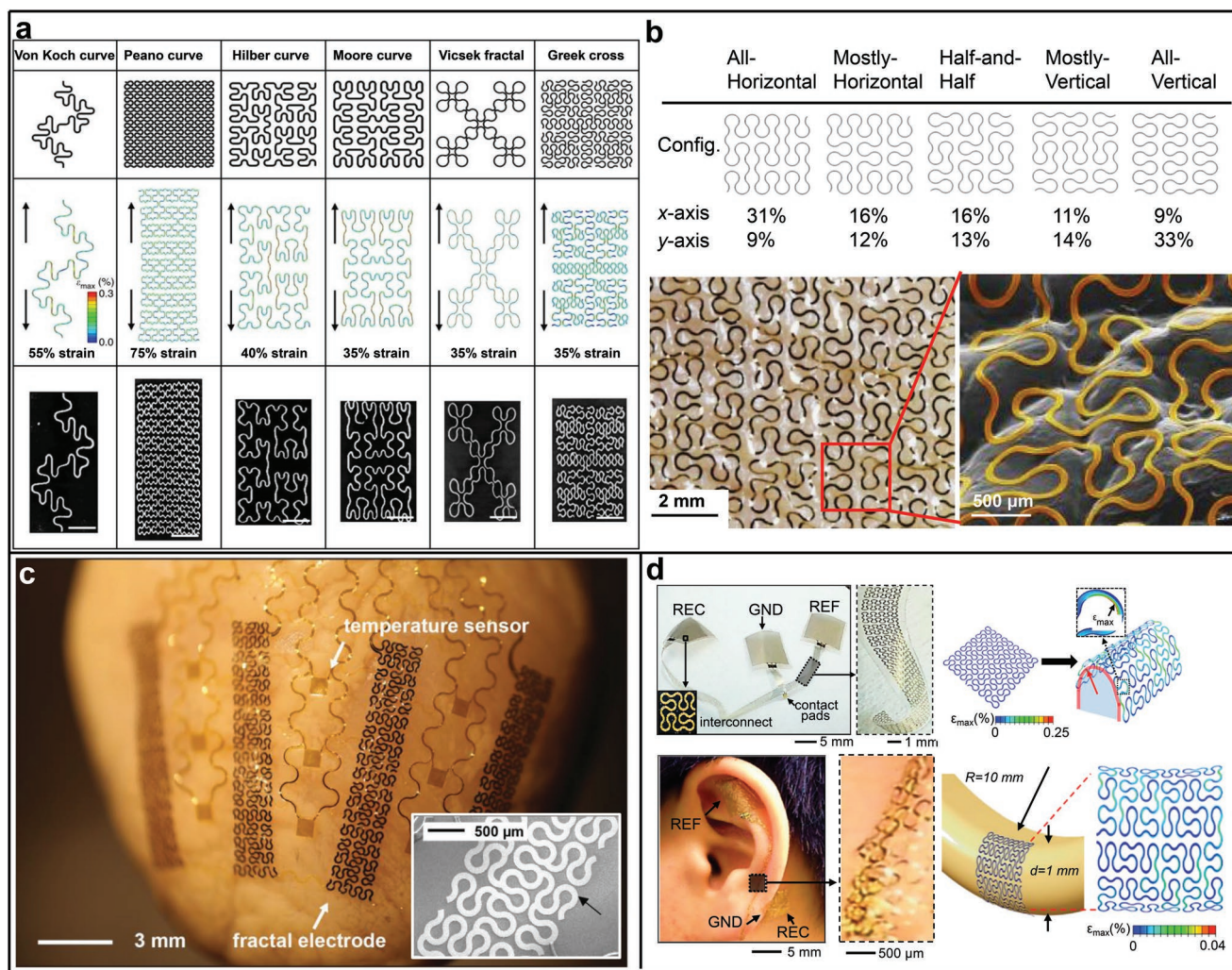


Figure 8. Fractal-inspired interconnects designs. a) Representative fractal layouts and their FEA, MicroXCT images under elastic tensile strains. Scale bars are 2 mm. b) Top panels: Calculated stretchability of five different second-order Peano layouts of metal wires mounted on an elastomer, given the maximum principal strain criterion is 0.3%. Bottom panels: Optical and SEM images of the third-order Peano layout of metal wires on skin and a skin-replica, respectively, showing the conformal contact with the skin. Reproduced with permission.^[154] Copyright 2014, Nature Publishing Group. c) Optical image of the fractal electrode array distributed over a rabbit heart circumference to deliver cardiac electrical stimulation, and sense cardiac electrical activity. Inset: SEM image of the fractal electrode. Reproduced with permission.^[152] Copyright 2015, Wiley-VCH. d) EEG devices in fractal layout and the corresponding mechanical properties. Reproduced with permission.^[153] Copyright 2015, National Academy of Sciences.

temporally programmed electrical stimulation, across a large area of the epicardium. Moreover, fractal-inspired electrodes can be applied to conform to more complex biological surfaces, with an example shown in Figure 8d, in which the fractal electrode meshes are directly and chronically mounted on the complex surface topology of the auricle and the mastoid. These ultrathin fractal electrodes offer extreme levels of bendability and stretchability to conform to different regions of the auricle, thereby providing for high-fidelity and long-term capture of electroencephalograms (EEG). An important additional feature is that the fractal-inspired layouts can be tailored with orientation dependent stretchability to match the requirements of auricle integration, e.g., by exploiting all-vertical Peano curves to achieve enhanced levels of stretchability along their longitudinal axes.

2.4. Kirigami Strategy

Kirigami strategies, inspired by the art of paper cutting and folding, recently emerged as an additional class of methods to design stretchable inorganic electronics.^[157–161] As shown in the inset of Figure 9a, a widely used kirigami patterns consist of cuts with periodic parallel distributions. The result induces lateral buckling of the planar structure in response to the in-plane stretching, thereby leveraging these ribbon deformations to accommodate large macroscopic strains. The FEA results demonstrate that the applied load can be uniformly distributed throughout most regions of the kirigami sheet. As a result, despite the presence of multiple defect sites, the system offers improved tolerance to damage, where the electrical conductance of the kirigami sheet remains almost strain-invariant.^[162]

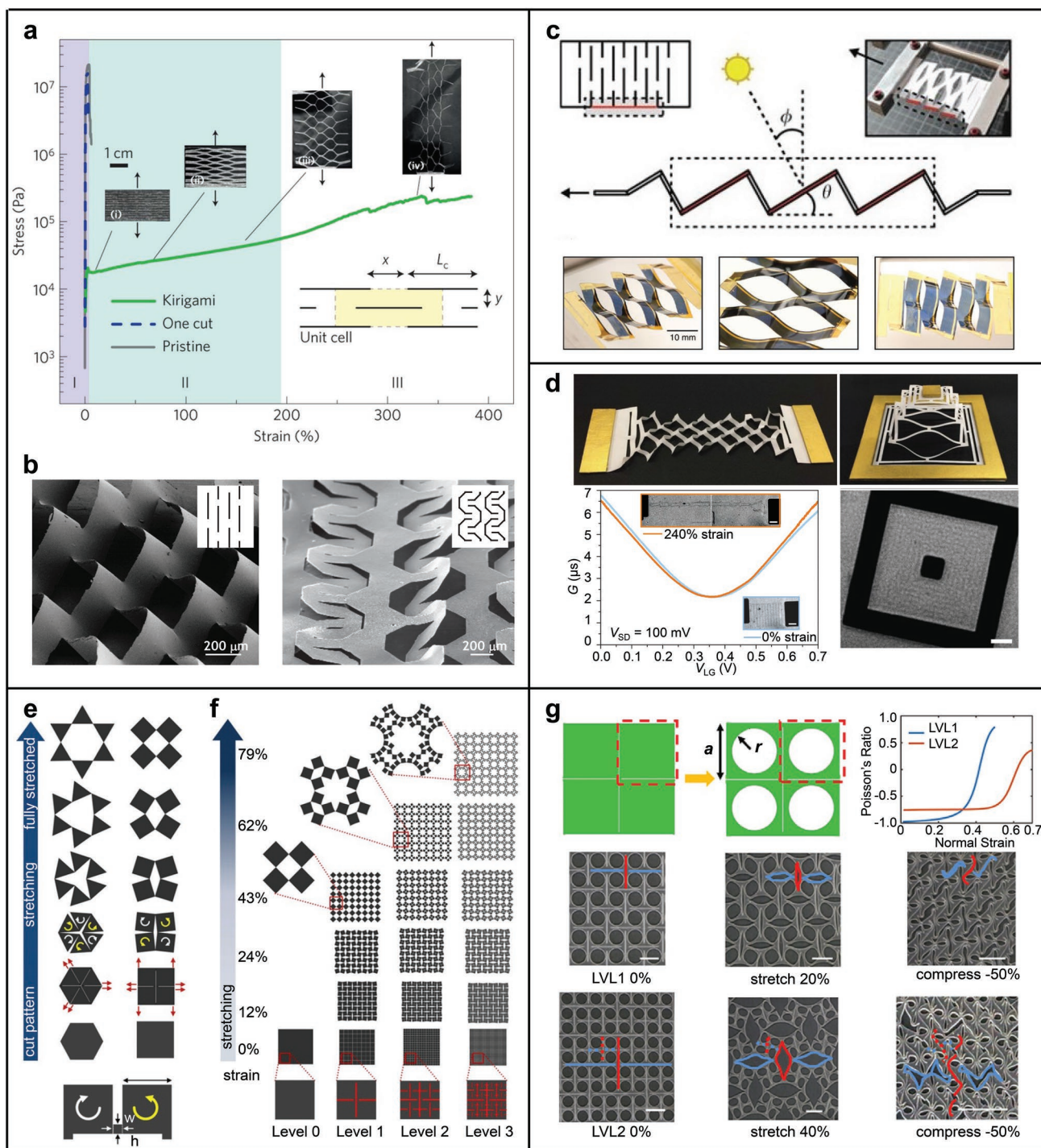


Figure 9. Kirigami strategy. a) Stress–strain curve for a kirigami sheet (green), a pristine sheet (gray) and a sheet with one-cut in the middle (blue). It exhibits markedly different deformation behaviors in three different regions, from initial elastic deformation to secondary elastic deformation with buckling, to pattern collapse. Insets are the illustration of the cut pattern for a unit cell, and SEM images (i–iv) of kirigami sheets corresponding to the different regions of the strain–stress curve. b) SEM images of two examples of kirigami patterns in graphene oxide/poly(vinyl alcohol) nanocomposites. The insets are the corresponding kirigami unit cells. Reproduced with permission.^[162] Copyright 2015, Nature Publishing Group. c) Schematic and photograph of a kirigami solar cell for dynamic sunlight tracking. Reproduced with permission.^[163] Copyright 2015, Nature Publishing Group. d) Stretchable graphene kirigami structure and its electrical properties. Scale bars, 10 μm . Reproduced with permission.^[167] Copyright 2015, Nature Publishing Group. e) Schematic of an in-plane rotation kirigami designs. The planar materials are cut and separated, enabling in-plane rotations with stretching. f) Schematic of a hierarchical fractal kirigami design. Subdivide units are obtained by repeating the cut pattern within the original one. Reproduced with permission.^[144] Copyright 2014, National Academy of Sciences. g) Schematic illustration and experimental images of a kirigami design with simultaneous stretchability and compressibility by introducing circular cut-outs to the solid square units. Reproduced with permission.^[173] Copyright 2017, Elsevier.

Based on this simple kirigami geometry, Figure 9a shows the stress–strain curves for a macroscale kirigami patterned sheet with one cut in the middle, and a nonpatterned sheet. The data exhibits markedly different deformation behaviors in three different regions, from the initial elastic deformation, to secondary elastic deformation with buckling, to pattern collapse. Figure 9b demonstrates two examples of kirigami patterns in graphene oxide/poly(vinyl alcohol) nanocomposites, with insets that show the corresponding kirigami unit cells.

The kirigami strategy was also utilized in structural designs of stretchable functional devices. For example, Lamoureux et al.^[163] developed an integrated solar tracking system, where a thin-film GaAs solar cell module is stretched to produce out-of-plane tilt to track the direction of incident sunlight, thereby maximizing the solar power generation. As shown in Figure 9c, the geometry of this dynamic tracking response system is precisely controlled by the out-of-plane buckling of kirigami structure, which suggests a pathway toward new applications for solar power. Compared to conventional solar tracking systems that rely on a complex assembly of mechanical components, the kirigami design strategy simplifies the actuation scheme and significantly reduces the weight and cost of the system. Based on the kirigami strategy, many other applications were also demonstrated recently, such as flexible mechanical metamaterials,^[163] wide-angle diffraction gratings,^[164] ultrastretchable bioprobes,^[165] and stretchable lithium–ion batteries,^[166] providing either novel functions or enhanced physical properties.

It is interesting to note that the kirigami concept can be applied to a wide range of dimension scales. Inspired by the geometric similarity of paper and 2D materials, the ideas in the paper model can be extended to 2D materials, such as graphene. As shown in Figure 9d, graphene kirigami has been demonstrated,^[167] where the graphene sheet can be assembled into 3D configurations in a manner similar to a paper model, through the in-plane or out-of-plane loading. Since the graphene crystal lattice itself does not experience significant strain during the deformation, the electrical properties (e.g., the conductance curves) in the unstretched and stretched states remain unchanged. The kirigami inspired shapes of graphene show excellent mechanical robustness and extremely high stretchability ($\approx 240\%$), suggesting possibilities for developing highly stretchable electronics based on the graphene or other 2D materials.

Apart from the out-of-plane deformations under stretching, the kirigami strategy also enables in-plane rotations of the components in response to in-plane stretching.^[168–171] The essence of this kirigami design is to divide the planar structure into rotating units by strategic cutting patterns,^[44,172] as exemplified in Figure 9e. The rotating units (e.g., triangles or squares) between the slits are rigid, and the connections between these units appear to be (almost) freely rotating the hinge, such that the deformations of the structure (e.g., under biaxial and uniaxial stretching) primarily occur by the rotations of the units, rather than by the significant deformations of the units themselves. The final form, dependent on the cutting pattern, is determined mainly by the moment equilibrium. For any specific cut patterns, the maximum stretch ratio (strain) can be achieved by rotation, beyond which the units themselves deform. As shown in Figure 9e, each unit rotates clockwise or counterclockwise,

resulting in an expansion of the original structure under equal-biaxial stretching. With a simple unit rotation, the expansion continues to reach a maximum level, or until the moment balances and the structures are fully extended. If the material of the units is rigid, the units cannot be further expanded. Moreover, based on the geometry of rotating units, fractal concepts have also been introduced to improve the stretchability, as exemplified in Figure 9f, where the units are hierarchically subdivided into smaller units by repeating the cut pattern within the original ones. In this fractal kirigami design, the expansion at lower level is largely exhausted before the expansion at the higher level begins, and higher orders of fractal iterations result in a larger deformability of the kirigami sheets. Meanwhile, due to the same cutting pattern over the entire structure, the allowable rotation angle of the smallest units becomes limited. However, this limitation can be addressed by alternately cutting the pattern between horizontal planes, allowing the smallest units to achieve a larger angle of rotation, thereby improving the maximum stretchability. This fractal kirigami design can expand the design space of structural materials so that they can be adapted for diverse applications.

Although these kirigami designs offer large stretchabilities, most of them show very limited compressibility. Recently, circular cut-outs were introduced into the solid square cut units of the kirigami design,^[173] to allow large tension and compression, simultaneously. As shown in Figure 9g, the circular cut-outs enable the structure to accommodate up to 50% compression via buckling-induced full compactness of the pores, while the line cuts enable a large stretchability via the rotation of the porous units.

3. Structural Designs of Substrates

Flexible substrates represent a very important component of stretchable inorganic electronics. Many studies have focused on the design of the substrates to provide specific application platforms, e.g., to realize the strain-isolation of the rigid devices from the substrate deformations,^[174–178] to improve biocompatibility and conformability to biological tissues,^[36,47,179–182] or to develop innovative applications with fundamentally new features and functionalities.^[26,27] In this section, we highlight a few representative structural designs of substrates, including the surface structure designs, cellular substrate designs, and curvilinear substrate designs.

3.1. Surface Structure Designs

In the widely used island-bridge designs as discussed above, the introduction of stretchable interconnects reduces the effective areal coverage of the systems, which could decrease the device performance and integration level, especially for optoelectronic devices like solar cell and photodetectors. To solve this problem, the surface microrelief designs for the substrate were proposed to realize the strain-isolation of the electronics from the deformations of the substrate, while achieving a high areal coverage,^[176,183,184] as shown in Figure 10a. The microrelief design involves the use of isolated islands (raised regions)

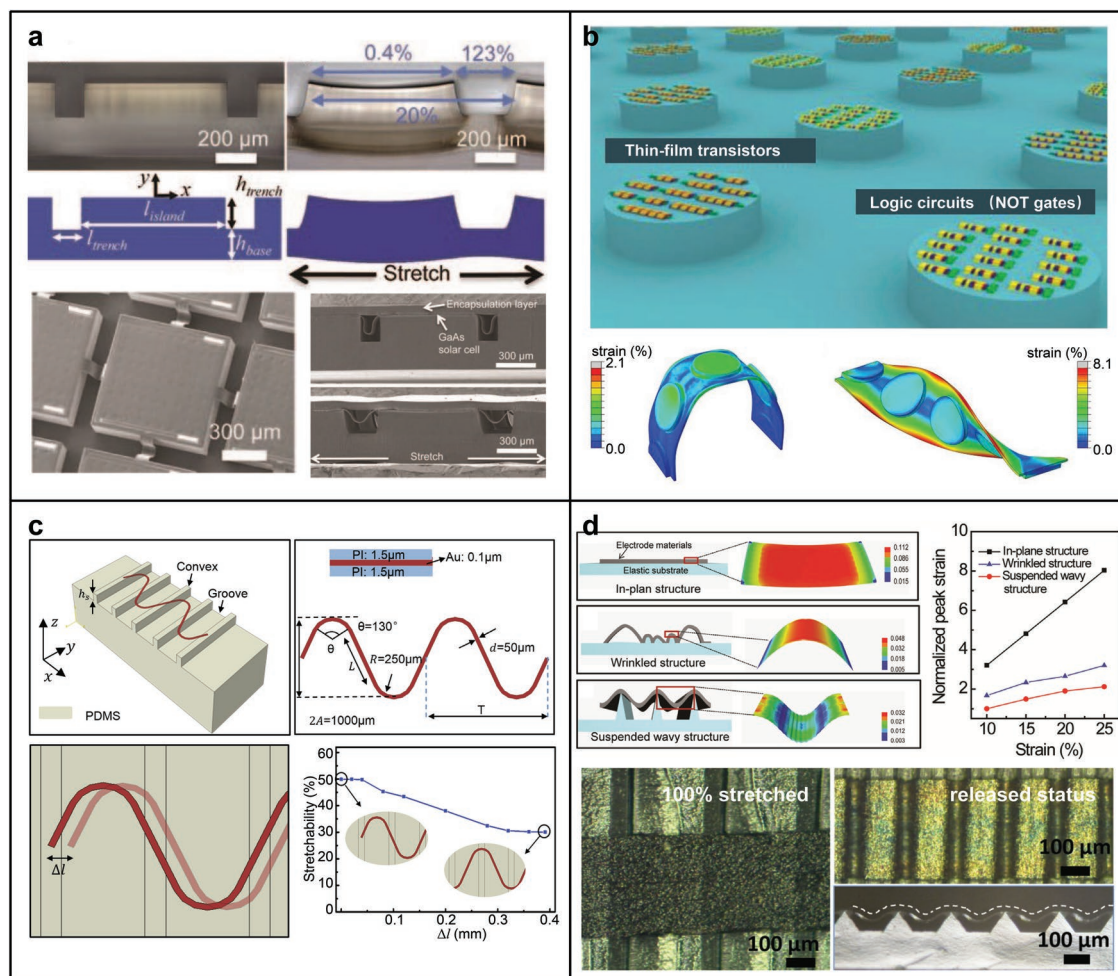


Figure 10. Surface structure designs. a) Top panels: Optical microscopy images and FEA results of the PDMS in surface substrate microrelief design. Bottom panels: SEM images of stretchable GaAs photovoltaic modules with interconnects. Reproduced with permission.^[176] Copyright 2011, Wiley-VCH. b) Top panel: Schematic illustration of TFTs and inverters fabricated directly on the raised regions of a mesa-shaped substrate. Bottom panel: Strain distribution of the mesa-shaped elastomeric substrate under different deformations (i.e., bending ≈ 6 mm in radius, and twisting at 180°). Reproduced with permission.^[185] Copyright 2018, Wiley-VCH. c) Schematic illustration of toothed substrate design with serpentine interconnects integrated (top left). Geometric parameters of serpentine interconnects (top right). Illustration of position offset between serpentine interconnects and toothed substrates (bottom left). The influence of position offset on stretchability of serpentine interconnects (bottom right). Reproduced with permission.^[186] Copyright 2018, Wiley-VCH. d) Top panels: Schematic of various electrode arrays (i.e., in-plane structure, wrinkled structure, and suspended wavy structure). The FEA results indicate their relevant strain distributions and the peak strains. Bottom panels: Optical images of the micro-supercapacitors in 100% stretched and released status and its cross-sectional image. Reproduced with permission.^[190] Copyright 2015, Wiley-VCH.

to place the functional device, and recessed trenches to accommodate the buckling deformations of interconnects. Additional optimizations of the island shapes and layouts can further improve the stretchability and the effective areal coverage, e.g., by replacing the square islands with notched islands.^[184]

Moreover, the design of high-relief structures with mesa shapes can minimize the strain on the electronics, as shown in Figure 10b, where thin-film transistors (TFTs) and logic circuits (inverters) can be integrated.^[185] Here, the use of such high-relief structures is intended to localize the applied strains on the substrate, around the mesas, rather than on their surfaces. As a result, the device can withstand different modes of deformation, e.g., bending up to 6 mm radius, 20% uniaxial strain, and 180° global twisting, while showing stable electrical performances.

In addition to the role of strain isolation, substrates with such surface structure designs can also enable relative freestanding deformations of serpentine interconnects, for example, by use of toothed substrate,^[186] as presented in Figure 10c. This toothed design aims to eliminate the mechanical constraints of the substrate on the serpentine interconnects. Specifically, under uniaxial stretching, the portion of the serpentine interconnects that do not contact the substrate are not restricted in their motions when deformed, such that the stretchability of the integrated system improves and potential damage to the interconnects by adhesion constraints to the substrate can be avoided. Indeed, the position deviation of the serpentine interconnects to the toothed substrate may lead to a reduction of the stretchability, but the reduction is modest according to FEA, as shown in the bottom panel of Figure 10c.

The tripod design is another type of surface structure that decreases the strain in stretchable inorganic electronic systems.^[43,187,188] Here, the thin film is suspended to the substrate, which significantly decreases the stress caused by the physical contact, as shown in the Figure 10d. As with the wavy designs introduced in Section 2.1, this structure can be fabricated by transferring a thin film on a prestrained substrate with tripod structure, followed by release of the prestrain. The FEA results show that suspended 2D wavy structures can further reduce strain concentrations in electrode fingers, as compared to the in-plane and wrinkled structures, as shown in the top panels of Figure 10d, such that detaching and cracking of the electrode materials can be prevented. This design can be applied to many different thin-film devices, e.g., electrodes in bio-integrated electronics^[189] and graphene microribbons in micro-supercapacitors.^[190]

3.2. Cellular Substrate Designs

Figure 11a presents a type of honeycomb cellular design in an elastomer substrate integrated with a stretchable array of ion sensors, with demonstrated applications in bio-integrated electronics.^[179] The open cellular construct consists of porous features to transport fluids and planar structures to mount sensor arrays (Figure 11a), thereby allowing fluids to diffuse through the low modulus thin substrate, while maintaining a tight integration with the sensors. This substrate design can facilitate the exchange of biofluids for monitoring the biomarkers, by minimizing cumulative artifacts caused by the impermeability of conventional substrates. Experimental measurements and theoretical simulations elucidated the underlying mechanics associated with these systems (Figure 11b), including cases when the sensor arrays with serpentine interconnects were mounted on open cellular and solid substrates. The results showed that the pores in the open cellular substrate do not constrain the buckling of the serpentine interconnects, and that the introduction of these structures reduces the maximum strain in Au (serpentine interconnects) from 12% to 1% compared to the solid case, leading to significantly enhanced stretchability. The overall elastic properties of such systems are often difficult to determine precisely, because they strongly depend on the detailed alignment and position of the serpentine interconnects relative to the pores in the cellular substrate, at levels that can be difficult to control experimentally.^[191] Figure 11c shows a schematic illustration of finite-deformation mechanics model for the open honeycomb cellular substrate. Specifically, Chen et al.^[192] established an analytic constitutive model by considering the cellular substrate as an equivalent medium. For serpentine interconnects bonded to this equivalent medium, many variables affect the mechanical responses, such as the relative direction and position, and Figure 11d shows a representative geometric model. The analyses showed that the lower bound of the elastic stretchability can be estimated by analyzing the serpentine interconnect bonded to the equivalent medium. Figure 11e,f illustrates the influence of the geometric parameters on the elastic stretchability, which is important in considering various design options.

In bio-integrated applications, the mechanical properties of the thin substrate can be tuned by tailoring the microstructure

geometries to match those of tissues or skins, form improved biocompatibility and conformability. Jang et al.^[136] developed a network design strategy of in soft, lithographically defined composites (Figure 11g) that can quantitatively reproduce the mechanics of biological materials, including the nonlinear stress–strain responses of human skin and its subtle spatial variations across different locations on the body. As shown in Figure 11h, the network designs can be implemented to precisely match the J-shaped stress–strain curves of human skins at different region (e.g., back and abdomen area). In this network design, both the geometries of the horseshoe microstructure in an epoxy polymer and the lattice topology can be tailored to yield the desired nonlinear mechanical responses.

Figure 11i presents three examples, including a hierarchical triangular lattice, hierarchical kagome lattice, and hierarchical honeycomb lattice, all with sixfold rotational symmetry. Development of a theoretical model allows a clear understanding of the microstructure–property relationship in such types of network composite materials designs. Four key parameters, the elastic modulus, transition strain, peak tangent modulus, and peak strain, characterize the “J-shaped” stress–strain curves of the lattice network. The models provide accurate predictions of these parameters as well as the deformed configurations. For example, as shown in Figure 11j for a hierarchical triangular lattice, the theoretical, FEA and experiment results of “J-shaped” stress–strain curves with different geometric parameters are in good agreement.^[193] Therefore, the “J-shaped” stress–strain behavior can be controlled by inverse design of the geometric parameters, to precisely match those of human skin or other biological tissues.^[194]

Furthermore, matching the Poisson's ratio of the network substrates to the skin can increase the comfort level of the system, which has important applications in biomedical devices.^[195] Liu et al.^[196] developed a network design strategy for soft structural materials, which can yield tailored isotropic Poisson's ratio from -1 to 1 , with a tunable strain range from 0% to $\approx 90\%$. This design relies on a network construction in a periodic lattice topology, which incorporates zigzag microstructures as building blocks to connect the lattice nodes. Figure 11k shows a schematic illustration of the design concepts and the geometries of the network materials. The theoretical design methods define tailored network geometries to yield target Poisson ratios with desired strain ranges. Figure 11l demonstrates an example of an optimized design of artificial skin, whose negative Poisson's ratio and nonlinear stress–strain curve reproduce well with those of the skin of a cat, as an example. The results suggest many potential applications of this design strategy in tissue engineering and bio-integrated devices.

3.3. Curvilinear Substrate Designs

Curvilinear electronic systems, typically integrated with a curvilinear substrate, are of growing interest, where the shapes create unusual opportunities for device applications with fundamentally new features and enhanced functionality.^[197–200] A main challenge is that conventional microfabrication techniques apply well to flat surfaces but they are intrinsically incompatible with complex curvilinear surfaces. Stretchable

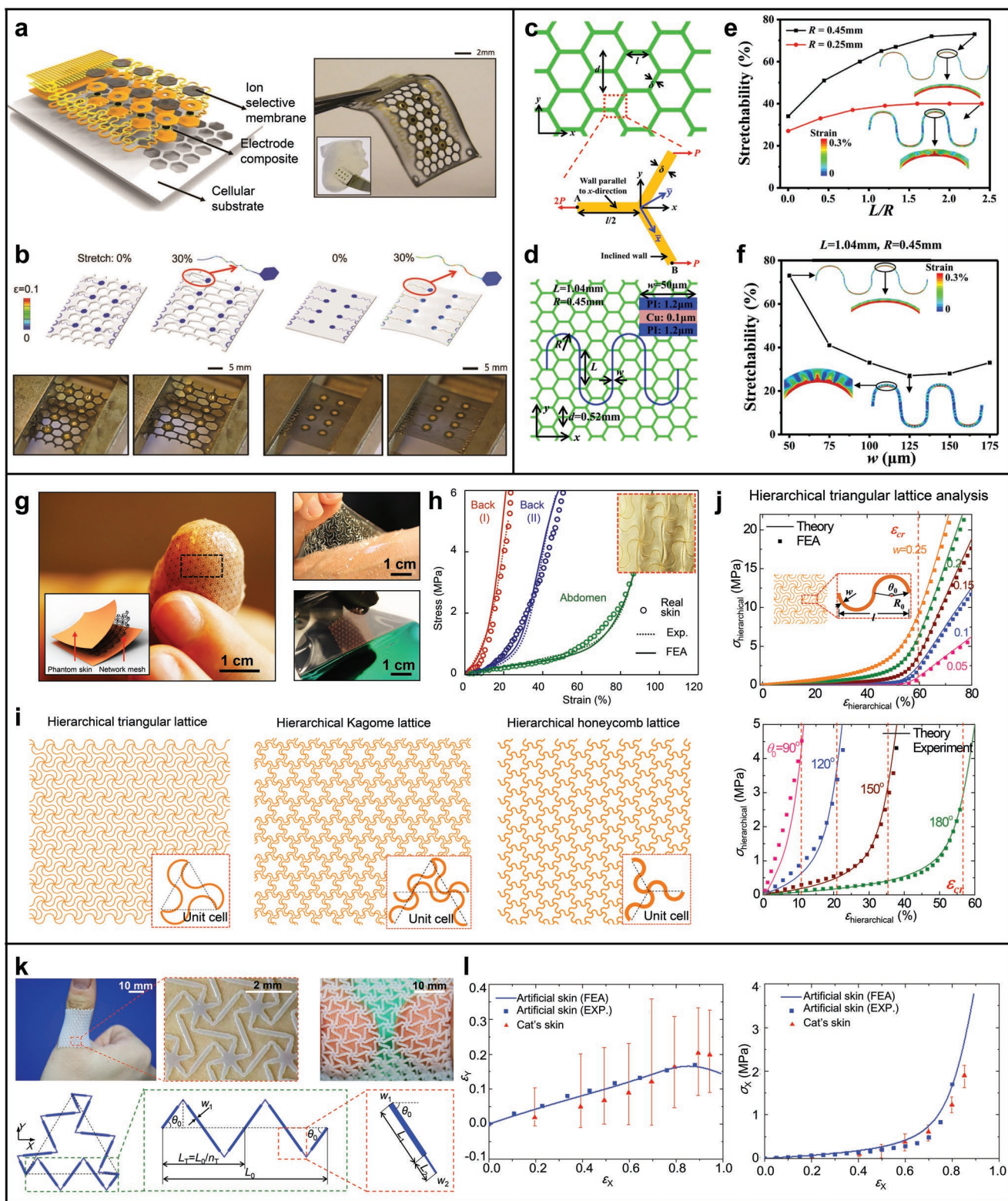


Figure 11. Cellular substrate designs. a) Schematic illustration and photograph of ion selective sensors on a honeycomb cellular substrate. b) FEA results and optical images of the ion sensor integrated onto cellular (top left, bottom left) and solid (top right, bottom right) substrates, under 30% uniaxial stretching. Reproduced with permission.^[179] Copyright 2017, Wiley-VCH. c) Geometrical parameters of the honeycomb cellular substrate, and the mechanics model of a unit cell. d) Geometric model of a serpentine interconnects bonded to the cellular substrate. e, f) The relationship between the elastic stretchability of serpentine interconnects and the geometrical parameters (i.e., length-to-radius ratio L/R , width w , as noted in d)). The interconnects are bonded onto the cellular substrates. Reproduced with permission.^[192] Copyright 2018, Elsevier. g) Optical images of a network design

inorganic electronic devices with structural designs allow integration of advanced high-performance 2D planar electronic circuits onto arbitrarily curvilinear surfaces, with a representative example shown in **Figure 12a**, highlighting hemispherical compressible silicon optoelectronics.^[26]

The hemispherical substrate is one of the most widely studied curvilinear substrates, because of significant applications in imaging systems, since the hemispherical shape enables a larger depth of field, wider viewing angle and lower aberrations with simple lensing systems compared to the traditional planar case.^[201–203] As an example, **Figure 12b** shows an electronic camera inspired by the human eye.^[26] Furthermore, the arthropod eye with in hemispherical, compound apposition layouts has additional unique advantages in wide-angle field of view, high acuity to motion and an infinite depth of field, compared to the human eye with a single or dual lens imaging principles. Inspired by this biological structure, Song et al.^[27] developed arthropod-inspired digital cameras that combine elastic microlens components with a stretchable thin silicon photodetector array, as shown in **Figure 12c**. Imaging systems of the future might incorporate such designs for advanced applications in industrial inspection, surveillance and others.

Another advantage of hemispherical imaging systems is their ability to match strongly nonplanar image surfaces, where Petzval curvature can lead to strongly nonplanar shapes. The fixed curvatures of the early systems of this type do not allow, however, dynamic changes in the Petzval surface that occur with adjustable zoom magnification, for example. To overcome this limitation, a dynamically tunable hemispherical camera system was developed,^[204] where the deformable digital imaging device was built by utilizing photodetector arrays on thin elastic membranes that can deform reversibly into hemispherical shapes with dynamically tunable radii of curvature. As shown in **Figure 12d**, this camera system combines a deformable digital imaging device with a similarly tunable, fluidic plan convex lens, thereby yielding a hemispherical camera with variable zoom and excellent imaging characteristics. Systematic experimental and theoretical studies of the mechanics and optics reveal all underlying principles of the operation.^[205]

Deformable curved substrates can also be form fitted to the complex surfaces encountered in biology to enable a conformal integration with stretchable electronic systems.^[206,207] Kim et al. developed instrumented deformable balloon catheters that integrate diverse stretchable functional sensors and actuators to provide multimodal functionality suitable for clinical uses as advanced surgical tools (**Figure 12e**).^[180] **Figure 12f** provides a demonstration of this device system that involves an impedance-based contact sensor integrated on a collapsible balloon catheter to assess the degree of contact with a target tissue.^[208]

The contact and noncontact conditions shown in the X-ray image are consistent with the inflation and deflation cycling of the balloon and the signal changes of impedance-based sensors.

4. Structural Designs for Spatial Integration of Device Systems

Stretchable electronics in 3D forms have received increasing attention in recent years, because of the enhanced level of integration and the new functionalities enabled by the spatial layouts. This section highlights a few representative structural designs in this context, covering the strategies of folding-based origami, buckling-guided 3D assembly, and stacked multilayer assembly.

4.1. Strategy of Folding-Based Origami

Origami, an ancient art of paper folding, is utilized to create 3D structures by folding flat sheets along strategic creases following predefined sequences,^[209–212] which has been recently explored for applications in many engineering fields, e.g., compactly deployable solar arrays for space applications,^[209] self-folding crawling robots for machine manufacturing,^[213] and cardiac stents for biomedical applications.^[214] Since structural transformations based on origami concepts are mostly determined by the kinematics associated with the geometrical parameters, which is basically scale-independent, this concept can be applied to a wide range of length scales, from nanoscale to meter scale, and even larger.^[209,215–218]

In practical applications of stretchable inorganic electronics, recent progress demonstrated that 3D transformations based on origami strategies can provide a stretchable platform for the integration of active devices and functional components.^[219–224] Miura-ori is one of the most extensively studied origami strategies,^[225] and the kinematics of Miura-ori from unfold to semi-fold to fold (**Figure 13a**) show that the facets between the creases is strain-free, which can be applied as the integration platform to mount active devices. **Figure 13b** illustrates a unit cell of Miura-ori and the associated key geometric parameters. When modeled as rigid origami, the Miura-ori sheet with a single in-plane kinematics mode can be characterized by the Poisson's ratio

$$\nu_{SL} = -\frac{\varepsilon_L}{\varepsilon_S} = -\frac{S}{L} \frac{dL}{dS} = -\tan^2 \xi = -\cos^2 \theta \tan^2 \gamma \quad (12)$$

where ε_L and ε_S are the instantaneous true strains. Based on Equation (12), **Figure 13b** plots the relation of the Poisson's ratio

strategy of soft composites, which can quantitatively reproduce the mechanics of biological materials. h) FEA and experimental results of stress–strain responses of human skin (circles) and the network design based soft composites (dot lines) of different individuals (person I–III). Inset: Optical image of the as-fabricated network design based soft composites. Reproduced with permission.^[6] Copyright 2015, Nature Publishing Group. i) Three representative examples of the network designs, i.e., hierarchical triangular lattice (left), hierarchical kagome lattice (middle) and hierarchical honeycomb lattice (right). Insets are the corresponding unit cells. j) Theoretical, FEA and experimental results of the stress–strain curves for the network based designs based on a hierarchical triangular lattice. Top panel: stress–strain curves for several normalized widths (\bar{w}) at fixed arc angle of $\theta_0 = 180^\circ$. Bottom panel: stress–strain curves for several arc angles (θ_0) at fixed normalized width of $\bar{w} = 0.15$. Reproduced with permission.^[193] Copyright 2016, Elsevier. k) Schematic illustration of a network based design with tailored isotropic negative Poisson's ratios. l) Negative Poisson's ratio and nonlinear stress–strain curves of artificial skins (FEA and experiments) and cat's skin (experiments). Reproduced with permission.^[196] Copyright 2018, Royal Society of Chemistry.

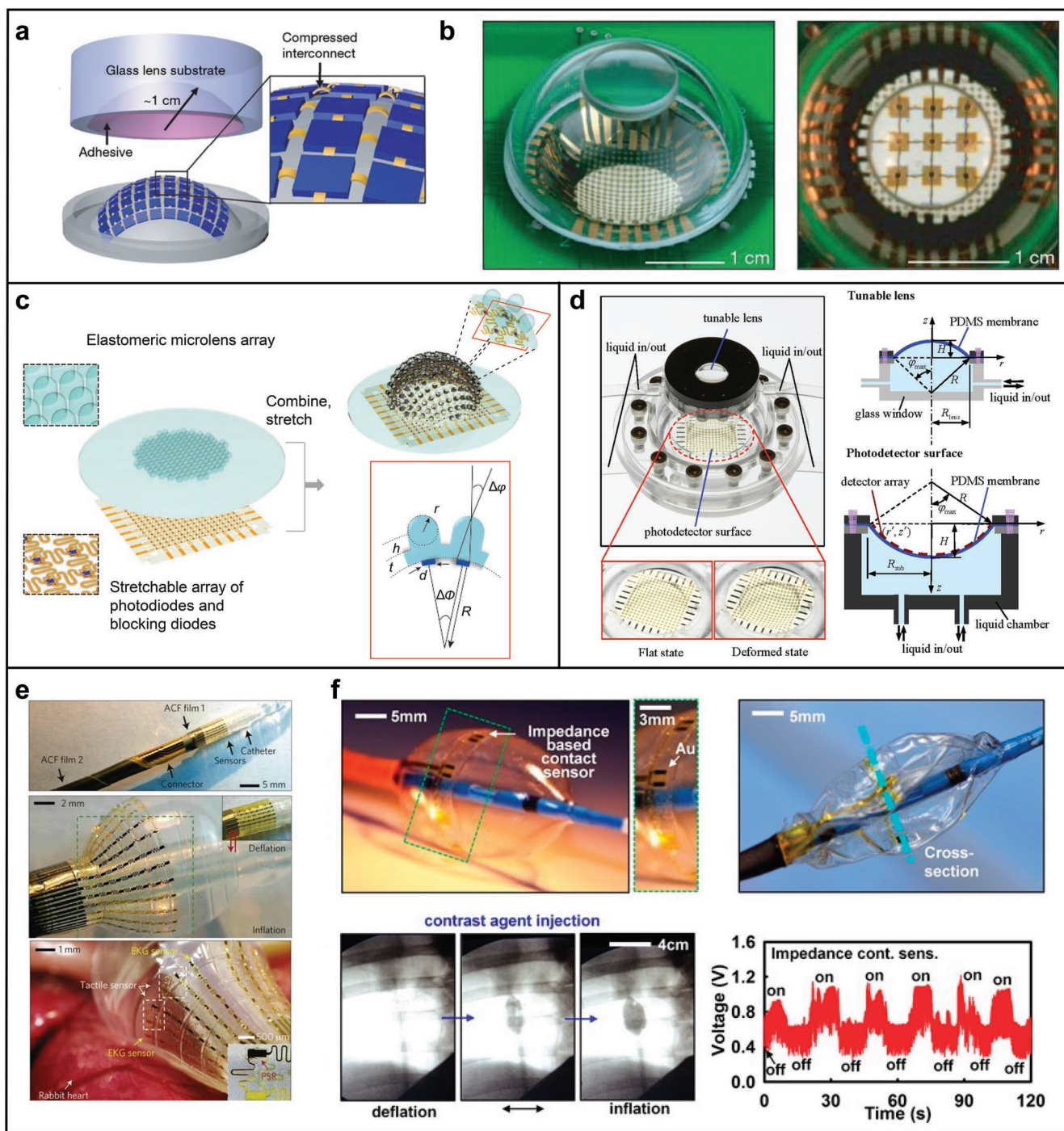


Figure 12. Curvilinear substrate designs. a) Schematic of compressible silicon optoelectronics conformally wrapped onto a hemispherical substrate. b) Photographs of a hemispherical electronic camera inspired by human eye. Reproduced with permission.^[26] Copyright 2008, Nature Publishing Group. c) Schematic illustrations of arthropod-inspired digital cameras, fabricated by combining an elastic microlens component with the stretchable thin silicon photodetector array. Reproduced with permission.^[27] Copyright 2013, Nature Publishing Group. d) A dynamically tunable hemispherical camera system. Left panels: Photographs of a camera system with tunable lens and a photodetector array. Angled views of the tunable photodetector surface in flat and deformed states. Right panels: Schematic illustrations of the deformation of the tunable lens. The tunability of this photodetector deformation is achieved via water extraction. Reproduced with permission.^[25] Copyright 2013, ASME. e) Optical images of a multifunctional inflatable balloon catheter integrated with tactile and electrogram sensors. Reproduced with permission.^[180] Copyright 2011, Nature Publishing Group. f) Top panel: Optical images of a collapsible balloon catheter integrated with impedance-based contact sensor webs both in inflated and deflated states. Bottom left panel: X-ray images of balloon catheter in conditions of contact and noncontact with the nearby superior vena cava, in a live porcine model. Bottom right panel: The in vivo tests of impedance contact sensors. Reproduced with permission.^[208] Copyright 2012, National Academy of Sciences.

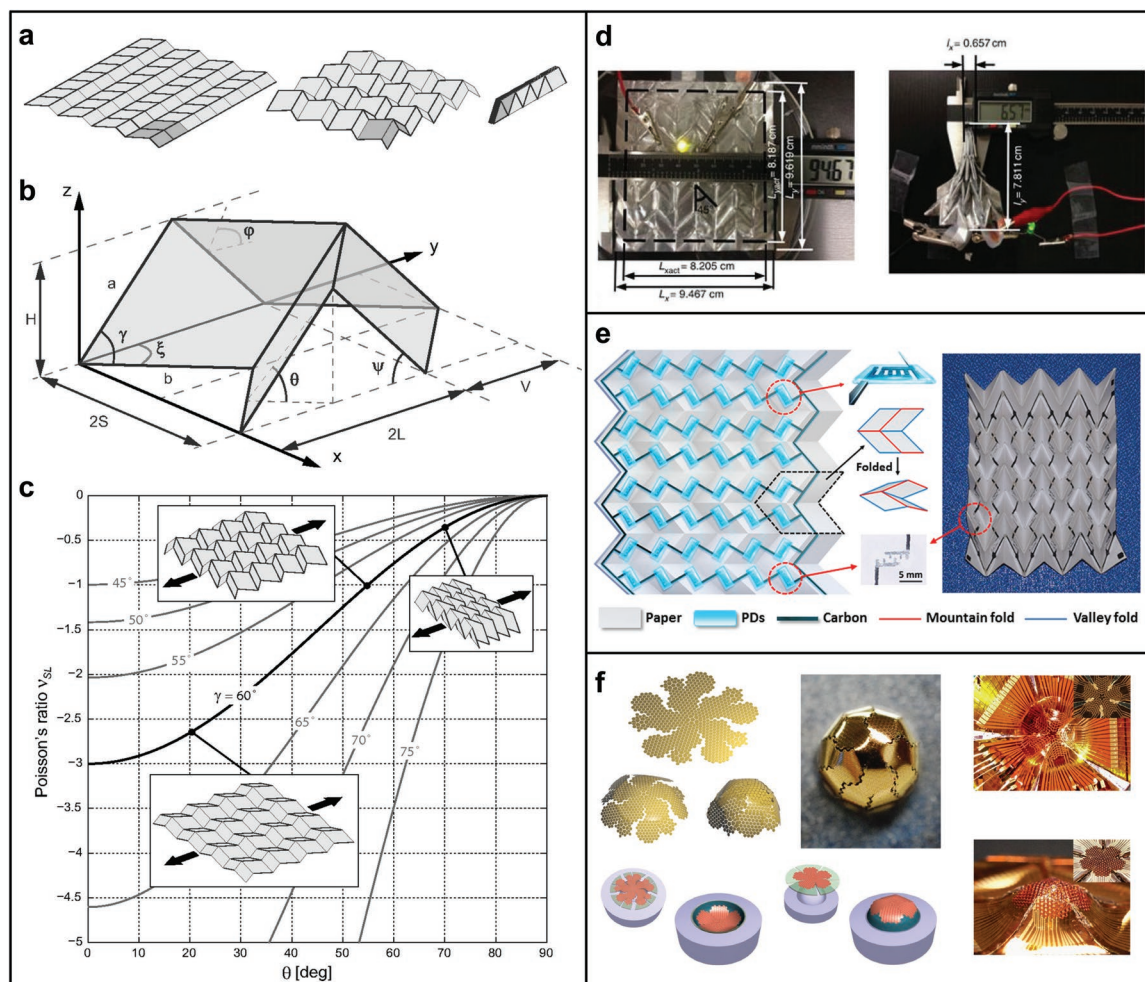


Figure 13. Folding-based origami strategy for spatial integration. a) The kinematics of Miura-ori from unfolded to semifolded to folded state. b) Miura-ori and the geometrical parameters of its unit cell. c) The relation of the Poisson's ratio and the fold angle θ for the different parallelogram. Reproduced with permission.^[225] Copyright 2013, National Academy of Sciences. d) Photographs of an origami battery in the completely unfolded and completely compressed state, respectively. Reproduced with permission.^[42] Copyright 2014, Nature Publishing Group. e) Schematic of the origami structure with the integration of ZnO photodetector array in a completely unfolded state. Reproduced with permission.^[227] Copyright 2017, American Chemical Society. f) Schematic illustration of the fabrication process for the hemispherical electronic eye by the strategy of folding-based origami. Reproduced with permission.^[228] Copyright 2017, Nature Publishing Group.

and the fold angle θ for different parallelogram (i.e., different angle γ). The Poisson's ratio is always negative, suggesting an excellent foldability and deployability.

Miura-ori patterns with high levels of deformability have important applications in energy harvesting and storage,^[42,220,226] photodetection,^[227] etc. In particular, origami lithium-ion batteries have been demonstrated,^[42,226] as shown in Figure 13c, in which the working battery is in the completely unfolded and completely compressed states. This origami battery exhibits stable and reliable performances under large cycles of mechanical deformations. Based on the integration techniques of Miura-ori origami, stretchable and deformable origami paper photodetector arrays (OPPDA) were developed by utilizing printable ZnO nanowires and carbon electrodes.^[227] Figure 13e illustrates that the ZnO photodetector unit cells are mounted at the center of each parallelogram. Since the tessellated parallelograms can be oriented in four

different directions, the OPPDA offers excellent capabilities of omnidirectional photodetection. The origami strategy also allows the integrated OPPDA to withstand repeated stretching, bending, and twisting, without any obvious performance degradation.

In addition, an origami-inspired approach was developed to fabricate dense, scalable, and compact hemispherical electronic eye systems,^[228] which is compatible with existing complementary metal-oxide-semiconductor (CMOS) sensor technologies that allow arrangements in an extremely high density. As shown in Figure 13f, with each polygon block serving as a sensor pixel, silicon-based photodetector arrays shaped into a truncated icosahedral pattern were fabricated on flexible sheets, and further folded into a concave or convex hemisphere. This example demonstrates the important application potential of the origami strategy as a spatial integration platform to develop next generation stretchable/flexible electronics.

4.2. Strategy of Buckling-Guided 3D Assembly

As compared to folding-based origami strategies, recently developed assembly methods guided by controlled buckling can access to more sophisticated 3D geometries, owing to the versatility of complex deformation modes, precursor designs, and loading strategies. These methods are applicable to a broad set of material types (e.g., metal, semiconductor, soft polymers) and feature scales (e.g., from nanometers to centimeters) in high-speed, because of the full compatibility with the conventional microfabrication technologies.^[139,140,229,230]

As described in Section 2.2.4, regarding the fabrication process of helical interconnects, the buckling-guided 3D assembly relies on a prestrained elastomer substrate to serve as the platform, to allow a controlled 2D-to-3D transformation, after the release of the prestrain in the substrate.^[169] **Figure 14a–d** presents an example that exploits this strategy to build 3D stretchable multifunctional photodetectors.^[231] The 3D structure after the release of the prestrain (46%) is shown in **Figure 14a**. The interconnects of the device exploit a sandwich construction, with the graphene encased by two SU-8 layers, as illustrated in the colored SEM images of **Figure 14b**. The SU-8 layers are buckled into a hemispherical structure, allowing a 3D arrangement of the MoS₂ patches that serve as photodetecting elements. One of the advantages arises from this form of 3D integration is the capability to allow the tracking of both the direction and intensity of the incident light, as shown in **Figure 14c**. Additionally, the atomically thin MoS₂ and graphene enable an optically transparent device system, such that the light is able to pass through the device for detection at two sensing regions, from which the incident angles can be determined. Note that this cannot be easily achieved by photodetector arrays in planar layouts. Photodetectors in other 3D geometries such as an octagonal prism and an octagonal prismoid can be also formed using this assembly strategy, as illustrated in **Figure 14d**. These devices can be reversibly stretched and buckled from 2D to 3D configurations, continuously, even under a large number of cyclic loadings, showing the robustness.^[231]

In addition to the 3D assembly based on the compressive buckling, a tensile buckling strategy can be also exploited to form 3D stretchable electronic systems, as a route to bypass the need of prestretching.^[232] As illustrated in **Figure 14e**, when the substrate is stretched uniaxially, the nonbonded regions of 2D precursor are delaminated from the substrate, resulting in a 3D transformation through coordinated bending/twisting deformations and translational/rotational motions. The ability to tune the 3D geometries of the devices assembled in this manner has practical applications, with an example presented in **Figure 14e**, showing a visible strain sensor array. This strain sensor offers a large detectable range, from $\approx 9.8\%$ to $\approx 50\%$. The spiral-shaped conducting ribbons represent the key enabling elements of this device, as the 3D transformation induced by the tensile buckling triggers the illumination of connected LEDs at targeted strains.

3D electrically small antennas (ESA), i.e., antennas much smaller as compared to the operating wavelength, provide an excellent electrical performance for applications in miniaturized communication systems.^[233–235] 3D ESAs provide another representative example, where the spatial integration of the device system is essential.^[236,237] It should be noted that the

planar ESAs are usually limited in performance attributes such as the efficiencies and the bandwidths, due to the small volume occupation of the Chu-sphere. The spatially integrated ESAs, such as hemispherical ESA, can ideally occupy the Chu-sphere, thereby offering substantially improved performance.^[238] **Figure 14f** shows a buckled meanderline-based hemispherical electrically small antenna (MHESA), whose quality factor is very close to its theoretical lower bound, according to both the results of experiments and simulations (**Figure 14g**). The deformability of the ESAs also enables reversible tunability of the quality factor and radiation efficiency (**Figure 14g,h**), controlled by applying different levels of biaxial strains.^[236]

In the buckling-guided assembly strategy, recent advances show that different releasing sequences and specially engineered precursor designs can trigger the stabilization of multiple, distinct 3D configurations. Such reversible transformations in geometrical layouts provide a route to reconfigurable 3D electronics.^[239] **Figure 14i** illustrates an array of silicon *n*-channel metal–oxide–semiconductor–field-effect-transistors (*n*-MOSFET) integrated with a bistable 3D platform.^[239] The simultaneous release of the biaxial prestrain results in a 3D tower-shaped structure with four supporting struts, which can be reshaped into a recessed well with similar struts by using sequential prestrain release. Since the maximum principal strain remains below the yielding strain, the shape-shifting process is reversible, capable of repetitive reconfiguration. The results of transistor characteristics indicate that the *I*–*V* curves remain nearly unchanged after switching between these shapes (**Figure 14j**). The versatile capabilities of the buckling-guided assembly strategy also enable promising applications in many other areas.^[240–242]

4.3. Stacked Multilayer Designs

Minimizing the size of device system and maximizing the integration density of the circuits represents a challenge for stretchable inorganic electronics. Integration of the functional components into stacked multilayer designs could well address the limitation of functional density that can be reached using the conventional single-layer design.^[155,243,244]

Figure 15a–c demonstrates an electronic skin with ultrathin, single crystalline silicon nanoribbon sensors, encompassing strain sensors, pressure sensors, humidity sensors, and electroresistive heaters.^[155] A schematic illustration of the stacked multilayer design in **Figure 15a** shows the arrangement of electronics and sensors, with magnified views in **Figure 15c**. Each sensor/actuator layer has individual interconnects connected with the data acquisition instruments. The via-hole structures are exploited for the electrical integration of each stacked layer, which can further simplify the connecting wires. Due to the stacked designs, the sensor arrays may mechanically interfere with each other. To avoid this issue, the staggered arrangement of sensors in different layers provides a possible solution to reduce such mechanical interactions.^[155]

Lee et al.^[245] introduced a folding-based stacked design to achieve a skin-mountable power management with high functional density, as illustrated in **Figure 15d**. The folding strategy yields a bilayer design with reduced lateral dimensions.

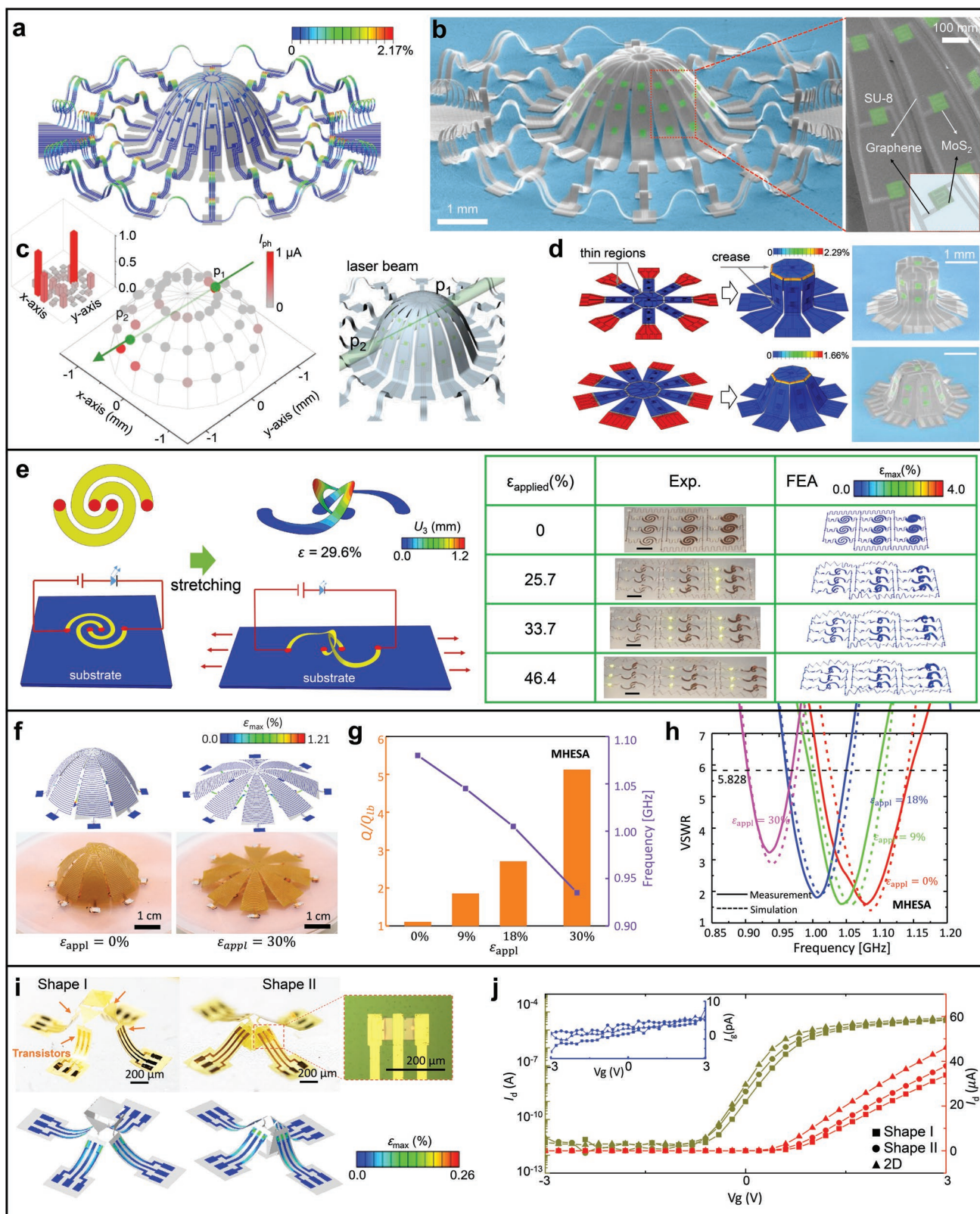


Figure 14. Buckling-guided 3D assembly strategy for spatial integration. a) FEA result of the 3D stretchable multifunctional photodetectors after compressive buckling assembly, indicating the distribution of maximum principal strains. b) Colored SEM images of photodetectors composed of MoS₂ patches (green), graphene interconnects (light gray), and SU-8 scaffold (gray). c) Photocurrent distribution on hemisphere surface, when a laser beam penetrating at two points of the 3D surface. d) Cases of an octagonal prism (top) and an octagonal prismoid (bottom), are assembled from

The FEA results on the folding process of wrapping, aligning, and pressing stages in Figure 15e indicate that even the strains in the most severely deformed regions are much smaller than the yielding strain of copper (0.3%), as noted in Figure 15f.^[245] The soft core material accommodates severe deformations, such that electronic interconnects mainly undergo bending deformations, resulting in ultralow strains. One of the challenging issues of this folding strategy is related to the relatively bulky and stiff devices that might allow conformal integration with soft, curvilinear surfaces, due to the increased system thickness. Xu et al. conducted a detailed study of the stretchable electronics in stacking layout, and defined a set of guidelines for optimizing the deformable properties.^[243]

Huang et al. reported a framework for stacking pre-designed functional devices and interconnects layer-by-layer into a highly integrated, stretchable system.^[246] Figure 15g shows a stretchable four-layer layout, where each layer is designed into “island-bridge” patterns. A challenging issue in the stacked design is how to form reliable interlayer electrical connections. Vertical interconnect accesses (VIAs) were introduced and manufactured through laser ablation and controlled soldering to enable communication of different layers, as shown in Figure 15h. The resulting multilayer system offers a good mechanical robustness and stretchability, according to the experimental measurements. The stress concentration around the chips results in a nonuniform strain in adjacent layers, as indicated in Figure 15j.^[246]

5. Conclusion and Outlook

This review summarizes some of the most important advances in mechanically guided structural designs for stretchable inorganic electronics, covering those of the device systems and the soft substrates, as well as the integration schemes. Consistent with other relevant reviews,^[43,91,247–251] this article also highlights the importance of unusual layouts and integration strategies for advanced electronic materials and devices to yield outstanding performance both in mechanical properties and electrical characteristics.

In the structural design of stretchable devices and systems, many critical factors must be considered for practical applications, including mechanical properties (e.g., stretchability and elastic modulus), areal coverage, encapsulation method, fabrication process (e.g., cost and compatibility), and etc. Wavy designs are mainly applicable for systems with less than 20% stretchability. Island-bridge layouts, due to the utility of different interconnect configurations (e.g., arc-shape, serpentine, 2D spiral, fractal and 3D helices), offer expanded options in design parameters to enhance the stretchability (> 100%, and even ≈1000%) at the

system level, thereby increasing the range of applications. Fractal-inspired design and kirigami strategies are both capable of achieving large stretchability and high areal coverage, with unique applications in sensing, optoelectronic, and energy harvesting/storage, where high levels of integration and/or energy densities are required. In most cases, the solid encapsulation materials that protect against chemical and physical damage restrict deformations of the flexible features of the systems, thereby reducing their stretchability, especially for layouts based on “in-plane” structures (e.g., serpentine interconnect, 2D spiral interconnect, fractal-inspired design, kirigami sheet). With “out-of-plane” structures (e.g., arc-shaped interconnect, 3D helical interconnect), the influence of the encapsulation on stretchability is reduced, due to the nature of the deformations that occur within the soft encapsulation material.

To provide specific platforms for targeted applications, structural substrates can be useful. For example, substrates with surface structures can provide strain-isolation of rigid devices from overall deformations of the system. Cellular substrates can improve the biocompatibility and conformability to biological tissues. Curvilinear substrates can enable innovative applications with fundamentally new features and functionalities. Opportunities exist in the design of structural substrates to provide advanced platforms that expand the scope of applications for stretchable inorganic electronics.

The three integration strategies discussed in this review offer distinct advantages relevant to different situations. The stacked multilayer design represents a scheme to assemble circuits layer by layer, corresponding to a 2.5D design framework. In comparison to stacked multilayer designs, folding-based origami and buckling-guided 3D assembly can achieve more complex 3D configurations, but typically with large amounts of hollow spaces. As a result, stacked multilayer designs can provide a higher integration density of functional components than these other two strategies. Specific 3D geometries (e.g., hemispheres) can offer important capabilities in some applications of electronics and optoelectronics, such as 3D electrically small antennas and photodetecting devices. In these and other cases, the folding-based origami and buckling-guided 3D assembly schemes can address requirements more effectively than stacked designs. As compared to the folding-based origami method, which is irreversible in most cases and is applicable mainly to 3D geometries with relatively sharp edges, the buckling-guided 3D assembly scheme offers access to a broad range of 3D geometries, through more sophisticated spatial deformations and translations/rotations, mostly in a reversible manner.

Despite this significant progress, challenges remain, especially in structural designs to enable enhanced levels of comfort and minimally invasive bio-integration and to offer a high

2D to 3D systems. Mechanical analysis is described in FEA results and the corresponding final configurations are presented in colored SEM images. Reproduced with permission.^[231] Copyright 2018, Nature Publishing Group. e) 3D mesostructures assembled by tensile buckling, with LED readout circuit served as sensors for strain visualization. Scale bars are 4 mm. Reproduced with permission.^[232] Copyright 2018, Springer Nature Publishing AG. f) Mechanical tunability of the MHESA under equal-biaxial tensile strains of 0% and 30%. g) The Q/Q_{1b} and center frequencies, h) voltage standing wave ratio (VSWR) characteristics of the MHESA under different stretching strains. Reproduced with permission.^[236] Copyright 2019, Wiley-VCH. i) 3D electronics with an array of silicon *n*-MOSFET integrated onto a reconfigurable bistable platform. j) Current–voltage (*I*–*V*) characteristics of the transistor in Shape I, Shape II and planar state. Reproduced with permission.^[239] Copyright 2018, Nature Publishing Group.

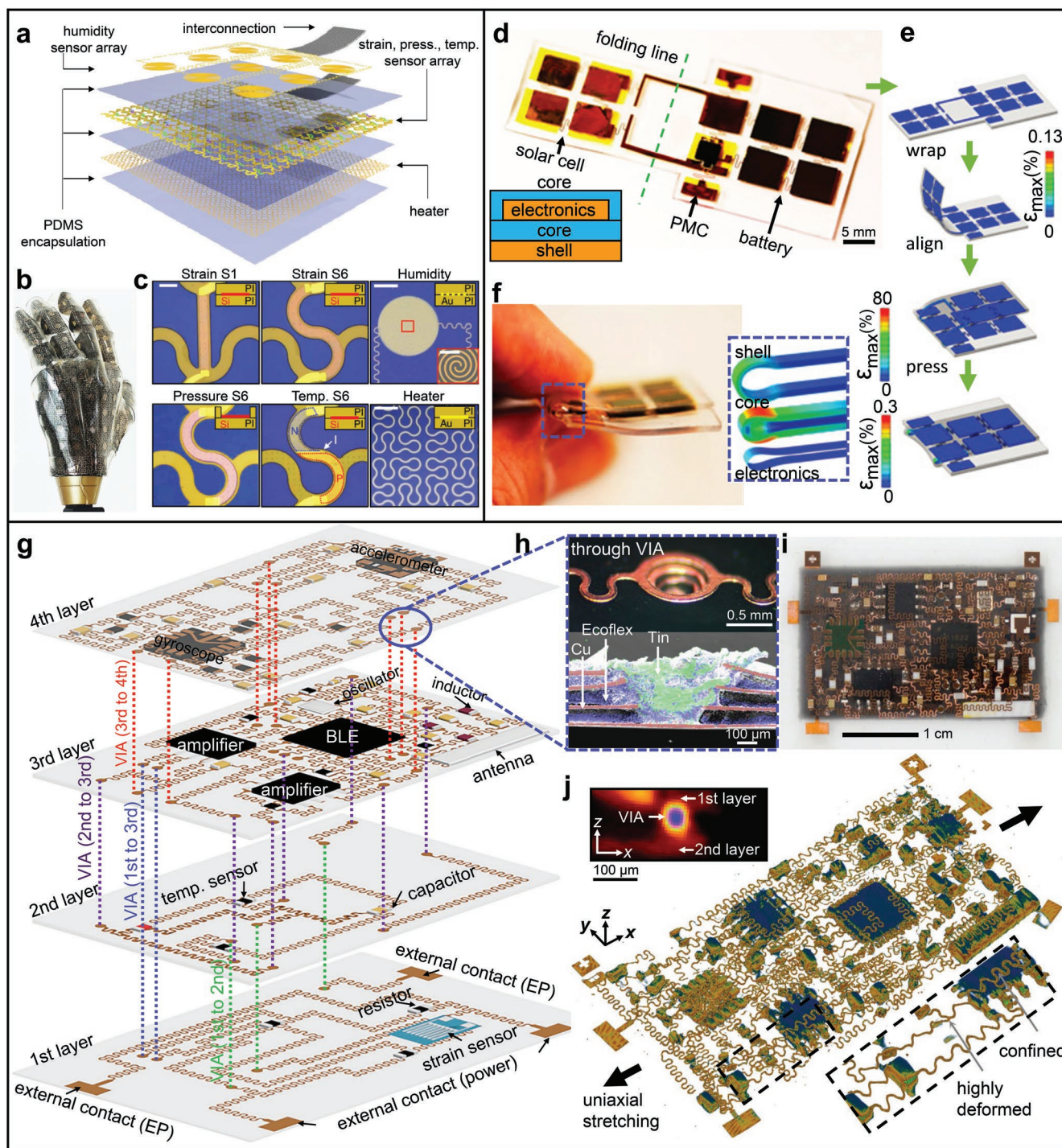


Figure 15. Stacked multilayer for spatial integration. a) An exploded view of the stacked multilayer electronic skin, which composed of six stacked layers. b) Picture of the electronic skin covering the surface of a prosthetic hand. c) Microscopic photograph of multifunctional sensors. Reproduced with permission.^[155] Copyright 2014, Nature Publishing Group. d) Images of solar cells and batteries integrated power control system stacked by folding. Inset: Cross-section view of a single layer. e) FEA results of the folding process. f) Photograph of the folded device and the enlarged view of FEA results for maximum strains near the folded region. Reproduced with permission.^[245] Copyright 2016, National Academy of Sciences. g) Design and exploded schematics of a four-layer-by-layer stacking integration system. h) Top: VIAs are used for interlayer connections. Bottom: Cross-section EDS (electron dispersive spectroscopy) image of the VIA. i) Photograph of the as-fabricated multilayer system. j) XCT (X-ray computed tomography) results of the multilayer circuits. Inset at top shows the cross-section of a VIA between adjacent layers. Inset at bottom illustrates the nonuniform deformation of Cu interconnects raised from the mechanical coupling of interlayers. Reproduced with permission.^[246] Copyright 2018, Nature Publishing Group.

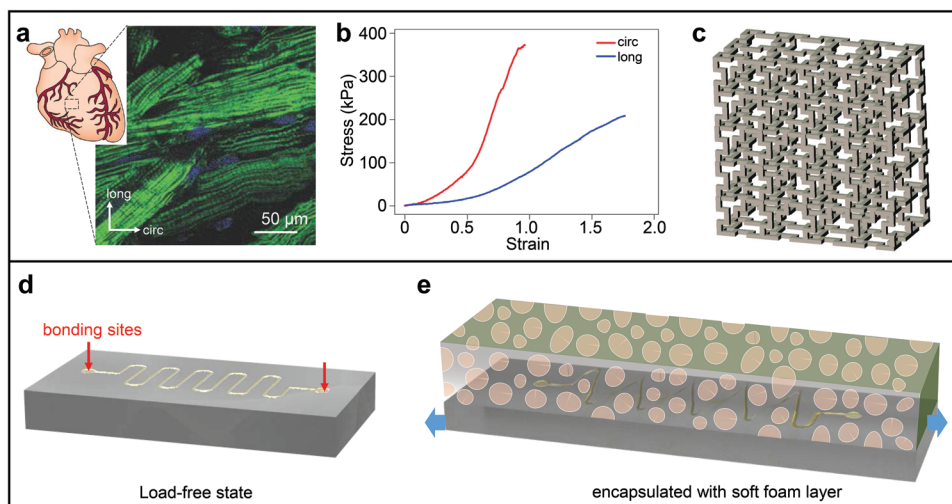


Figure 16. Challenge and outlook for stretchable inorganic electronics. a) A fluorescent specimen of an adult rat right ventricular myocardium indicating the preferential orientation of the cardiac muscle fibers. The circumferential (circ) and longitudinal (long) axes are noted. b) Uniaxial tensile stress–strain curves for circumferential and longitudinal directions of specimens noted in (b). Reproduced with permission.^[252] Copyright 2008, Nature Publishing Group. c) Schematic illustration of a type of architected 3D cellular substrate, which could offer anisotropic stress–strain responses to reproduce those of human tissues. d,e) Schematic illustration of architected encapsulants consisting of soft foams. The serpentine interconnect is bonded to the substrate at two ends, and uniaxially stretched to a predefined state before the encapsulation. Due to the ultralow stiffness of the soft foams, their mechanical constraints on the 3D deformations of serpentine interconnects can be minimized during stretching.

degree of mechanical deformability after solid encapsulation. On one hand, stretchable electronic devices, when integrated with the human heart or other tissues, could potentially cause adverse effects, due to mechanical loads induced by the unmatched mechanical properties with the biological materials. For example, the ventricular myocardium exhibits anisotropic mechanical responses, with tensile mechanical properties dictated by cardiac muscle fiber orientation (Figure 16a,b).^[252] To resolve this issue, further studies mainly focus on developing structural substrate materials whose nonlinear, anisotropic stress–strain responses can precisely reproduce those of human tissues/organs in targeted applications, perhaps in a spatially variant manner.^[47] Cellular 3D microstructures are attractive choices in this regard, due to the excellent permeability and sufficient open spaces to integrate functional device components (Figure 16c). On the other hand, the encapsulation is indispensable in most practical applications, either to physically protect the surrounding tissues/organs, or to avoid the degradation of functional components due to the chemical reactions that can follow upon contact with biofluids. Existing solid encapsulation strategies, however, mostly cause a reduction in the deformability (especially the stretchability), as compared to the unencapsulated inorganic electronics. Development of structural encapsulants (with an example shown in Figure 16d,e) and/or novel integration schemes that can suppress mechanical interactions between the encapsulation layer and the inorganic devices/interconnects could provide a possible solution.

Acknowledgements

Z.X. and H.S. contributed equally to this work. Y.Z. acknowledges support from the National Natural Science Foundation of China (Grant Nos. 11672152 and 11722217), the Tsinghua National Laboratory for Information Science and Technology and the State Key Laboratory of

Digital Manufacturing Equipment and Technology, Huazhong University of Science and Technology (No. DMETKF2019005). Y.H. acknowledges support from the NSF (Grant No. CMMI1635443). Z.X. acknowledges support from the National Postdoctoral Program for Innovative Talents (Grant No. BX20180157), and China Postdoctoral Science Foundation (Grant No. 2018M641332). H.S. acknowledges support from China Postdoctoral Science Foundation (Grant No. 2019M650648).

Conflict of Interest

The authors declare no conflict of interest.

Keywords

inorganic electronics, mechanical design, soft electronics, stretchable electronics, structural designs

Received: April 8, 2019
Revised: May 27, 2019
Published online: July 26, 2019

- [1] J. A. Rogers, T. Someya, Y. Huang, *Science* **2010**, *327*, 1603.
- [2] D. H. Kim, N. S. Lu, R. Ghaffari, J. A. Rogers, *NPG Asia Mater.* **2012**, *4*, e15.
- [3] J. M. Nassar, J. P. Rojas, A. M. Hussain, M. M. Hussain, *Extreme Mech. Lett.* **2016**, *9*, 245.
- [4] J. Song, H. Jiang, Y. Huang, J. A. Rogers, *J. Vac. Sci. Technol., A* **2009**, *27*, 1107.
- [5] Y. G. Sun, J. A. Rogers, *Adv. Mater.* **2007**, *19*, 1897.
- [6] D. J. Lipomi, Z. A. Bao, *Energy Environ. Sci.* **2011**, *4*, 3314.
- [7] Y. Liu, M. Pharr, G. A. Salvatore, *ACS Nano* **2017**, *11*, 9614.
- [8] D. H. Kim, R. Ghaffari, N. Lu, J. A. Rogers, *Annu. Rev. Biomed. Eng.* **2012**, *14*, 113.

- [9] M. M. Hussain, Z. Ma, S. F. Shaikh, *Electrochem. Soc. Interface* **2018**, 27, 65.
- [10] C. Yan, P. S. Lee, *Small* **2014**, 10, 3443.
- [11] Y. Liu, K. He, G. Chen, W. R. Leow, X. Chen, *Chem. Rev.* **2017**, 117, 12893.
- [12] Q. Cao, J. A. Rogers, *Adv. Mater.* **2009**, 21, 29.
- [13] K. D. Harris, A. L. Elias, H. J. Chung, *J. Mater. Sci.* **2016**, 51, 2771.
- [14] M. L. Hammock, A. Chortos, B. C. Tee, J. B. Tok, Z. Bao, *Adv. Mater.* **2013**, 25, 5997.
- [15] D. H. Kim, J. Xiao, J. Song, Y. Huang, J. A. Rogers, *Adv. Mater.* **2010**, 22, 2108.
- [16] Z. W. Li, Y. Wang, J. L. Xiao, *Curr. Opin. Solid State Mater. Sci.* **2015**, 19, 171.
- [17] J. Li, J. Zhao, J. A. Rogers, *Acc. Chem. Res.* **2018**, 52, 53.
- [18] X. Wang, L. Dong, H. Zhang, R. Yu, C. Pan, Z. L. Wang, *Adv. Sci.* **2015**, 2, 1500169.
- [19] J. He, R. G. Nuzzo, J. A. Rogers, *Proc. IEEE* **2015**, 103, 619.
- [20] F. Ershad, K. Sim, A. Thukral, Y. S. Zhang, C. Yu, *APL Mater.* **2019**, 7, 031301.
- [21] J.-W. Jeong, W.-H. Yeo, A. Akhtar, J. J. S. Norton, Y.-J. Kwack, S. Li, S.-Y. Jung, Y. Su, W. Lee, J. Xia, H. Cheng, Y. Huang, W.-S. Choi, T. Bretl, J. A. Rogers, *Adv. Mater.* **2013**, 25, 6839.
- [22] W.-H. Yeo, Y.-S. Kim, J. Lee, A. Ameen, L. Shi, M. Li, S. Wang, R. Ma, S. H. Jin, Z. Kang, Y. Huang, J. A. Rogers, *Adv. Mater.* **2013**, 25, 2773.
- [23] D.-H. Kim, N. Lu, R. Ma, Y.-S. Kim, R.-H. Kim, S. Wang, J. Wu, S. M. Won, H. Tao, A. Islam, K. J. Yu, T.-i. Kim, R. Chowdhury, M. Ying, L. Xu, M. Li, H.-J. Chung, H. Keum, M. McCormick, P. Liu, Y.-W. Zhang, F. G. Omenetto, Y. Huang, T. Coleman, J. A. Rogers, *Science* **2011**, 333, 838.
- [24] L. Tian, B. Zimmerman, A. Akhtar, K. J. Yu, M. Moore, J. Wu, R. J. Larsen, J. W. Lee, J. Li, Y. Liu, B. Metzger, S. Qu, X. Guo, K. E. Mathewson, J. A. Fan, J. Cornman, M. Fatina, Z. Xie, Y. Ma, J. Zhang, Y. Zhang, F. Dolcos, M. Fabiani, G. Gratton, T. Bretl, L. J. Hargrove, P. V. Braun, Y. Huang, J. A. Rogers, *Nat. Biomed. Eng.* **2019**, 3, 194.
- [25] S. Wang, M. Li, J. Wu, D.-H. Kim, N. Lu, Y. Su, Z. Kang, Y. Huang, J. A. Rogers, *J. Appl. Mech.* **2012**, 79, 031022.
- [26] H. C. Ko, M. P. Stoykovich, J. Song, V. Malyarchuk, W. M. Choi, C.-J. Yu, J. B. Geddes Iii, J. Xiao, S. Wang, Y. Huang, J. A. Rogers, *Nature* **2008**, 454, 748.
- [27] Y. M. Song, Y. Xie, V. Malyarchuk, J. Xiao, I. Jung, K.-J. Choi, Z. Liu, H. Park, C. Lu, R.-H. Kim, R. Li, K. B. Crozier, Y. Huang, J. A. Rogers, *Nature* **2013**, 497, 95.
- [28] H. C. Ko, G. Shin, S. Wang, M. P. Stoykovich, J. W. Lee, D.-H. Kim, J. S. Ha, Y. Huang, K.-C. Hwang, J. A. Rogers, *Small* **2009**, 5, 2703.
- [29] H.-s. Kim, E. Brueckner, J. Song, Y. Li, S. Kim, C. Lu, J. Sulkin, K. Choquette, Y. Huang, R. G. Nuzzo, J. A. Rogers, *Proc. Natl. Acad. Sci. USA* **2011**, 108, 10072.
- [30] S.-I. Park, Y. Xiong, R.-H. Kim, P. Elvikis, M. Meitl, D.-H. Kim, J. Wu, J. Yoon, C.-J. Yu, Z. Liu, Y. Huang, K.-c. Hwang, P. Ferreira, X. Li, K. Choquette, J. A. Rogers, *Science* **2009**, 325, 977.
- [31] A. D. Mickle, S. M. Won, K. N. Noh, J. Yoon, K. W. Meacham, Y. Xue, L. A. McIlvried, B. A. Copits, V. K. Samineneni, K. E. Crawford, D. H. Kim, P. Srivastava, B. H. Kim, S. Min, Y. Shiuani, Y. Yun, M. A. Payne, J. Zhang, H. Jang, Y. Li, H. H. Lai, Y. Huang, S.-I. Park, R. W. Gereau, J. A. Rogers, *Nature* **2019**, 565, 361.
- [32] H. Zhang, P. Gutruf, K. Meacham, M. C. Montana, X. Zhao, A. M. Chiarelli, A. Vázquez-Guardado, A. Norris, L. Lu, Q. Guo, C. Xu, Y. Wu, H. Zhao, X. Ning, W. Bai, I. Kandela, C. R. Haney, D. Chanda, R. W. Gereau, J. A. Rogers, *Sci. Adv.* **2019**, 5, eaaw0873.
- [33] J. Yoo, S. Jeong, S. Kim, J. H. Je, *Adv. Mater.* **2015**, 27, 1712.
- [34] K. Tae-il, K. Rak-Hwan, J. A. Rogers, *IEEE Photonics J.* **2012**, 4, 607.
- [35] S.-W. Hwang, G. Park, H. Cheng, J.-K. Song, S.-K. Kang, L. Yin, J.-H. Kim, F. G. Omenetto, Y. Huang, K.-M. Lee, J. A. Rogers, *Adv. Mater.* **2014**, 26, 1992.
- [36] K. I. Jang, H. U. Chung, S. Xu, C. H. Lee, H. Luan, J. Jeong, H. Cheng, G. T. Kim, S. Y. Han, J. W. Lee, J. Kim, M. Cho, F. Miao, Y. Yang, H. N. Jung, M. Flavin, H. Liu, G. W. Kong, K. J. Yu, S. I. Rhee, J. Chung, B. Kim, J. W. Kwak, M. H. Yun, J. Y. Kim, Y. M. Song, U. Paik, Y. Zhang, Y. Huang, J. A. Rogers, *Nat. Commun.* **2015**, 6, 6566.
- [37] B. H. Kim, J.-H. Kim, L. Persano, S.-W. Hwang, S. Lee, J. Lee, Y. Yu, Y. Kang, S. M. Won, J. Koo, Y. K. Cho, G. Hur, A. Banks, J.-K. Song, P. Won, Y. M. Song, K.-I. Jang, D. Kang, C. H. Lee, D. Pisignano, J. A. Rogers, *Adv. Funct. Mater.* **2017**, 27, 1606008.
- [38] X. Ning, X. Yu, H. Wang, R. Sun, R. E. Corman, H. Li, C. M. Lee, Y. Xue, A. Chempakasseril, Y. Yao, Z. Zhang, H. Luan, Z. Wang, W. Xia, X. Feng, R. H. Ewoldt, Y. Huang, Y. Zhang, J. A. Rogers, *Sci. Adv.* **2018**, 4, eaat8313.
- [39] Z. Yan, T. Pan, M. Xue, C. Chen, Y. Cui, G. Yao, L. Huang, F. Liao, W. Jing, H. Zhang, M. Gao, D. Guo, Y. Xia, Y. Lin, *Adv. Sci.* **2017**, 4, 1700251.
- [40] M. Han, H. Wang, Y. Yang, C. Liang, W. Bai, Z. Yan, H. Li, Y. Xue, X. Wang, B. Akar, H. Zhao, H. Luan, J. Lim, I. Kandela, G. A. Ameer, Y. Zhang, Y. Huang, J. A. Rogers, *Nat. Electron.* **2019**, 2, 26.
- [41] D.-H. Kim, J. Song, W. M. Choi, H.-S. Kim, R.-H. Kim, Z. Liu, Y. Y. Huang, K.-C. Hwang, Y.-w. Zhang, J. A. Rogers, *Proc. Natl. Acad. Sci. USA* **2008**, 105, 18675.
- [42] Z. Song, T. Ma, R. Tang, Q. Cheng, X. Wang, D. Krishnaraju, R. Panat, C. K. Chan, H. Yu, H. Jiang, *Nat. Commun.* **2014**, 5, 3140.
- [43] K. J. Yu, Z. Yan, M. Han, J. A. Rogers, *npj Flexible Electron.* **2017**, 1, 4.
- [44] Y. Cho, J.-H. Shin, A. Costa, T. A. Kim, V. Kunin, J. Li, S. Y. Lee, S. Yang, H. N. Han, I.-S. Choi, D. J. Srolovitz, *Proc. Natl. Acad. Sci. USA* **2014**, 111, 17390.
- [45] Y. G. Sun, V. Kumar, I. Adesida, J. A. Rogers, *Adv. Mater.* **2006**, 18, 2857.
- [46] Z. Xue, M. Sun, T. Dong, Z. Tang, Y. Zhao, J. Wang, X. Wei, L. Yu, Q. Chen, J. Xu, Y. Shi, K. Chen, I. C. P. Roca, *Nano Lett.* **2017**, 17, 7638.
- [47] Y. Ma, X. Feng, J. A. Rogers, Y. Huang, Y. Zhang, *Lab Chip* **2017**, 17, 1689.
- [48] M. Melzer, D. Makarov, A. Calvimontes, D. Karnaushenko, S. Baunack, R. Kaltofen, Y. Mei, O. G. Schmidt, *Nano Lett.* **2011**, 11, 2522.
- [49] M. D. Dickey, *Adv. Mater.* **2017**, 29, 1606425.
- [50] N. Lu, *The Bridge* **2013**, 43, 31.
- [51] S. Gong, W. L. Cheng, *Adv. Electron. Mater.* **2017**, 3, 1600314.
- [52] Z. G. Xue, M. K. Xu, X. Li, J. Wang, X. F. Jiang, X. L. Wei, L. W. Yu, Q. Chen, J. Z. Wang, J. Xu, Y. Shi, K. J. Chen, P. R. I. Cabarrocas, *Adv. Funct. Mater.* **2016**, 26, 5352.
- [53] J. Song, X. Feng, Y. Huang, *Natl. Sci. Rev.* **2016**, 3, 128.
- [54] S. Choi, S. I. Han, D. Kim, T. Hyeon, D. H. Kim, *Chem. Soc. Rev.* **2019**, 48, 1566.
- [55] C. Cao, Y. Chu, Y. Zhou, C. Zhang, S. Qu, *Small* **2018**, 14, 1803976.
- [56] H. Jin, N. Matsuhisa, S. Lee, M. Abbas, T. Yokota, T. Someya, *Adv. Mater.* **2017**, 29, 1605848.
- [57] M. Drack, I. Graz, T. Sekitani, T. Someya, M. Kaltenbrunner, S. Bauer, *Adv. Mater.* **2015**, 27, 34.
- [58] R. Moser, G. Kettlgruber, C. M. Siket, M. Drack, I. M. Graz, U. Cakmak, Z. Major, M. Kaltenbrunner, S. Bauer, *Adv. Sci.* **2016**, 3, 1500396.
- [59] D. J. Lipomi, M. Vosgueritchian, B. C. K. Tee, S. L. Hellstrom, J. A. Lee, C. H. Fox, Z. Bao, *Nat. Nanotechnol.* **2011**, 6, 788.

- [60] A. D. Valentine, T. A. Busbee, J. W. Boley, J. R. Raney, A. Chortos, A. Kotikian, J. D. Berrigan, M. F. Durstock, J. A. Lewis, *Adv. Mater.* **2017**, *29*, 1703817.
- [61] F. Xu, Y. Zhu, *Adv. Mater.* **2012**, *24*, 5117.
- [62] S. Gong, W. Schwalb, Y. Wang, Y. Chen, Y. Tang, J. Si, B. Shirinzadeh, W. Cheng, *Nat. Commun.* **2014**, *5*, 3132.
- [63] N. Matsuhisa, D. Inoue, P. Zalar, H. Jin, Y. Matsuba, A. Itoh, T. Yokota, D. Hashizume, T. Someya, *Nat. Mater.* **2017**, *16*, 834.
- [64] S. Lee, A. Reuveny, J. Reeder, S. Lee, H. Jin, Q. Liu, T. Yokota, T. Sekitani, T. Isoyama, Y. Abe, Z. Suo, T. Someya, *Nat. Nanotechnol.* **2016**, *11*, 472.
- [65] A. Miyamoto, S. Lee, N. F. Cooray, S. Lee, M. Mori, N. Matsuhisa, H. Jin, L. Yoda, T. Yokota, A. Itoh, M. Sekino, H. Kawasaki, T. Ebihara, M. Amagai, T. Someya, *Nat. Nanotechnol.* **2017**, *12*, 907.
- [66] T. Sekitani, Y. Noguchi, K. Hata, T. Fukushima, T. Aida, T. Someya, *Science* **2008**, *321*, 1468.
- [67] K. Chen, W. Gao, S. Emaminejad, D. Kiriya, H. Ota, H. Y. Y. Nyein, K. Takei, A. Javey, *Adv. Mater.* **2016**, *28*, 4397.
- [68] D. Kiriya, K. Chen, H. Ota, Y. Lin, P. Zhao, Z. Yu, T.-j. Ha, A. Javey, *J. Am. Chem. Soc.* **2014**, *136*, 11188.
- [69] P. H. Lau, K. Takei, C. Wang, Y. Ju, J. Kim, Z. Yu, T. Takahashi, G. Cho, A. Javey, *Nano Lett.* **2013**, *13*, 3864.
- [70] Y. Lee, T.-S. Kim, S.-Y. Min, W. Xu, S.-H. Jeong, H.-K. Seo, T.-W. Lee, *Adv. Mater.* **2014**, *26*, 8010.
- [71] J. C. Yeo, H. K. Yap, W. Xi, Z. Wang, C.-H. Yeow, C. T. Lim, *Adv. Mater. Technol.* **2016**, *1*, 1600018.
- [72] M. D. Bartlett, N. Kazem, M. J. Powell-Palm, X. Huang, W. Sun, J. A. Malen, C. Majidi, *Proc. Natl. Acad. Sci. USA* **2017**, *114*, 2143.
- [73] P. Yong-Lae, M. Carmel, K. Rebecca, B. Phillippe, J. W. Robert, *J. Micromech. Microeng.* **2010**, *20*, 125029.
- [74] I. D. Joshipura, H. R. Ayers, C. Majidi, M. D. Dickey, *J. Mater. Chem. C* **2015**, *3*, 3834.
- [75] M. D. Bartlett, A. Fassler, N. Kazem, E. J. Markvicka, P. Mandal, C. Majidi, *Adv. Mater.* **2016**, *28*, 3726.
- [76] C. Ladd, J.-H. So, J. Muth, M. D. Dickey, *Adv. Mater.* **2013**, *25*, 5081.
- [77] S. Xu, Y. Zhang, L. Jia, K. E. Mathewson, K.-I. Jang, J. Kim, H. Fu, X. Huang, P. Chava, R. Wang, S. Bhole, L. Wang, Y. J. Na, Y. Guan, M. Flavin, Z. Han, Y. Huang, J. A. Rogers, *Science* **2014**, *344*, 70.
- [78] A. P. Gerratt, H. O. Michaud, S. P. Lacour, *Adv. Funct. Mater.* **2015**, *25*, 2287.
- [79] A. Hirsch, H. O. Michaud, A. P. Gerratt, S. de Mulatier, S. P. Lacour, *Adv. Mater.* **2016**, *28*, 4507.
- [80] S. Gupta, W. T. Navaraj, L. Lorenzelli, R. Dahiya, *npj Flexible Electron.* **2018**, *2*, 8.
- [81] N. S. Lu, D. H. Kim, *Soft Rob.* **2014**, *1*, 53.
- [82] Z. G. Xue, T. G. Dong, Z. M. Zhu, Y. L. Zhao, Y. Sun, L. W. Yu, *Journal of Semiconductors* **2018**, *39*, 011001.
- [83] X. T. Guo, S. S. Zheng, G. X. Zhang, X. Xiao, X. R. Li, Y. X. Xu, H. G. Xue, H. Pang, *Energy Storage Mater.* **2017**, *9*, 150.
- [84] D. H. Kim, J. A. Rogers, *Adv. Mater.* **2008**, *20*, 4887.
- [85] X. Yu, W. Shou, B. K. Mahajan, X. Huang, H. Pan, *Adv. Mater.* **2018**, *30*, 1707624.
- [86] Y. Zhang, L. Zhang, K. Cui, S. Ge, X. Cheng, M. Yan, J. Yu, H. Liu, *Adv. Mater.* **2018**, *30*, 1801588.
- [87] T. Someya, Z. Bao, G. G. Malliaras, *Nature* **2016**, *540*, 379.
- [88] M. A. Yoder, Z. Yan, M. Han, J. A. Rogers, R. G. Nuzzo, *J. Am. Chem. Soc.* **2018**, *140*, 9001.
- [89] Q. Guo, Z. Di, M. G. Lagally, Y. Mei, *Mater. Sci. Eng.: R: Rep.* **2018**, *128*, 1.
- [90] J. A. Rogers, M. G. Lagally, R. G. Nuzzo, *Nature* **2011**, *477*, 45.
- [91] A. J. Baca, J.-H. Ahn, Y. Sun, M. A. Meitl, E. Menard, H.-S. Kim, W. M. Choi, D.-H. Kim, Y. Huang, J. A. Rogers, *Angew. Chem., Int. Ed.* **2008**, *47*, 5524.
- [92] D. Y. Khang, J. A. Rogers, H. H. Lee, *Adv. Funct. Mater.* **2009**, *19*, 1526.
- [93] Y. Wang, Z. W. Li, J. L. Xiao, *J. Electron. Packag.* **2016**, *138*, 020801.
- [94] S. Yang, K. Khare, P.-C. Lin, *Adv. Funct. Mater.* **2010**, *20*, 2550.
- [95] S. Wang, J. Song, D.-H. Kim, Y. Huang, J. A. Rogers, *Appl. Phys. Lett.* **2008**, *93*, 013109.
- [96] C. J. Yu, Z. Y. Wang, H. Y. Yu, H. Q. Jiang, *Appl. Phys. Lett.* **2009**, *95*, 141912.
- [97] Q. T. Zhang, H. Yin, *J. Mech. Phys. Solids* **2018**, *118*, 40.
- [98] Y. Ma, Y. Xue, K. I. Jang, X. Feng, J. A. Rogers, Y. Huang, *Proc. R. Soc. A* **2016**, *472*, 20160339.
- [99] C. J. Yu, H. Q. Jiang, *Thin Solid Films* **2010**, *519*, 818.
- [100] Z. G. Yan, B. L. Wang, K. F. Wang, *Composites, Part B* **2019**, *166*, 65.
- [101] T. H. Kim, W. M. Choi, D. H. Kim, M. A. Meitl, E. Menard, H. Q. Jiang, J. A. Carlisle, J. A. Rogers, *Adv. Mater.* **2008**, *20*, 2171.
- [102] D. Y. Khang, H. Jiang, Y. Huang, J. A. Rogers, *Science* **2006**, *311*, 208.
- [103] H. Jiang, D. Y. Khang, J. Song, Y. Sun, Y. Huang, J. A. Rogers, *Proc. Natl. Acad. Sci. USA* **2007**, *104*, 15607.
- [104] W. M. Choi, J. Song, D. Y. Khang, H. Jiang, Y. Y. Huang, J. A. Rogers, *Nano Lett.* **2007**, *7*, 1655.
- [105] Y. Sun, W. M. Choi, H. Jiang, Y. Y. Huang, J. A. Rogers, *Nat. Nanotechnol.* **2006**, *1*, 201.
- [106] H. Y. Cheng, Y. H. Zhang, K. C. Hwang, J. A. Rogers, Y. G. Huang, *Int. J. Solids Struct.* **2014**, *51*, 3113.
- [107] H. Cheng, J. Song, *J. Appl. Mech.* **2014**, *81*, 024501.
- [108] J. Song, H. Jiang, Z. J. Liu, D. Y. Khang, Y. Huang, J. A. Rogers, C. Lu, C. G. Koh, *Int. J. Solids Struct.* **2008**, *45*, 3107.
- [109] H. Jiang, Y. Sun, J. A. Rogers, Y. Huang, *Appl. Phys. Lett.* **2007**, *90*, 133119.
- [110] H. Q. Jiang, D. Y. Khang, H. Y. Fei, H. Kim, Y. G. Huang, J. L. Xiao, J. A. Rogers, *J. Mech. Phys. Solids* **2008**, *56*, 2585.
- [111] C. Chen, W. Tao, Z. J. Liu, Y. W. Zhang, J. Song, *Theor. Appl. Mech. Lett.* **2011**, *1*, 021001.
- [112] H. Jiang, Y. Sun, J. A. Rogers, Y. Huang, *Int. J. Solids Struct.* **2008**, *45*, 2014.
- [113] Y. G. Sun, J. A. Rogers, *J. Mater. Chem.* **2007**, *17*, 832.
- [114] D. H. Kim, J. H. Ahn, W. M. Choi, H. S. Kim, T. H. Kim, J. Song, Y. Y. Huang, Z. Liu, C. Lu, J. A. Rogers, *Science* **2008**, *320*, 507.
- [115] J. Song, Y. Huang, J. Xiao, S. Wang, K. C. Hwang, H. C. Ko, D. H. Kim, M. P. Stoykovich, J. A. Rogers, *J. Appl. Phys.* **2009**, *105*.
- [116] R. Li, M. Li, Y. W. Su, J. Z. Song, X. Q. Ni, *Soft Matter* **2013**, *9*, 8476.
- [117] B. Wang, S. D. Wang, *Theor. Appl. Mech. Lett.* **2016**, *6*, 6.
- [118] S. D. Wang, J. L. Xiao, J. Z. Song, H. C. Ko, K. C. Hwang, Y. G. Huang, J. A. Rogers, *Soft Matter* **2010**, *6*, 5757.
- [119] A. Wang, R. Avila, Y. Ma, *J. Appl. Mech.* **2017**, *84*, 094501.
- [120] S. Yang, S. Qiao, N. Lu, *J. Appl. Mech.* **2016**, *84*, 021004.
- [121] T. Widlund, S. X. Yang, Y. Y. Hsu, N. S. Lu, *Int. J. Solids Struct.* **2014**, *51*, 4026.
- [122] D. Son, J. H. Koo, J. K. Song, J. Kim, M. Lee, H. J. Shim, M. Park, M. Lee, J. H. Kim, D. H. Kim, *ACS Nano* **2015**, *9*, 5585.
- [123] S. X. Yang, E. Ng, N. S. Lu, *Extreme Mech. Lett.* **2015**, *2*, 37.
- [124] Z. Fan, Y. Zhang, Q. Ma, F. Zhang, H. Fu, K. C. Hwang, Y. Huang, *Int. J. Solids Struct.* **2016**, *91*, 46.
- [125] S. X. Yang, B. Su, G. Bitar, N. S. Lu, *Int. J. Fract.* **2014**, *190*, 99.
- [126] L. Xiao, C. Zhu, W. Xiong, Y. Huang, Z. Yin, *Micromachines* **2018**, *9*, 392.
- [127] L. Xu, S. R. Gutbrod, A. P. Bonifas, Y. Su, M. S. Sulkin, N. Lu, H. J. Chung, K. I. Jang, Z. Liu, M. Ying, C. Lu, R. C. Webb, J. S. Kim, J. I. Laughner, H. Cheng, Y. Liu, A. Ameen, J. W. Jeong, G. T. Kim, Y. Huang, I. R. Efmov, J. A. Rogers, *Nat. Commun.* **2014**, *5*, 3329.
- [128] Y. Zhang, S. Xu, H. Fu, J. Lee, J. Su, K. C. Hwang, J. A. Rogers, Y. Huang, *Soft Matter* **2013**, *9*, 8062.
- [129] Y. H. Zhang, S. D. Wang, X. T. Li, J. A. Fan, S. Xu, Y. M. Song, K. J. Choi, W. H. Yeo, W. Lee, S. N. Nazaar, B. W. Lu, L. Yin, K. C. Hwang, J. A. Rogers, Y. G. Huang, *Adv. Funct. Mater.* **2014**, *24*, 2028.

- [130] Y. Su, X. Ping, K. J. Yu, J. W. Lee, J. A. Fan, B. Wang, M. Li, R. Li, D. V. Harburg, Y. Huang, C. Yu, S. Mao, J. Shim, Q. Yang, P. Y. Lee, A. Armonas, K. J. Choi, Y. Yang, U. Paik, T. Chang, T. J. Dawidczyk, Y. Huang, S. Wang, J. A. Rogers, *Adv. Mater.* **2017**, *29*, 1604989.
- [131] T. S. Pan, M. Pharr, Y. J. Ma, R. Ning, Z. Yan, R. X. Xu, X. Feng, Y. G. Huang, J. A. Rogers, *Adv. Funct. Mater.* **2017**, *27*, 1702589.
- [132] C. Lv, H. Yu, H. Jiang, *Extreme Mech. Lett.* **2014**, *1*, 29.
- [133] N. Alcheikh, M. M. Hussain, *2018 IEEE 13th Annu. Int. Conf. on Nano/Micro Engineered and Molecular Systems (NEMS)*, IEEE, Singapore **2018**, p. 607.
- [134] N. Alcheikh, S. F. Shaikh, M. M. Hussain, *Extreme Mech. Lett.* **2018**, *24*, 6.
- [135] W.-L. Sung, C.-C. Chen, K. Huang, W. Fang, *J. Micromech. Microeng.* **2016**, *26*, 025003.
- [136] K. Huang, R. Dinyari, G. Lanzara, J. Y. Kim, J. Feng, C. Vancura, F.-K. Chang, P. Peumans, *2007 IEEE Int. Electron Devices Meet.*, IEEE, Washington, D.C. **2007**, p. 217.
- [137] J. P. Rojas, A. Arevalo, I. G. Foulds, M. M. Hussain, *Appl. Phys. Lett.* **2014**, *105*, 154101.
- [138] M. U. Rehman, J. P. Rojas, *Extreme Mech. Lett.* **2017**, *15*, 44.
- [139] S. Xu, Z. Yan, K.-I. Jang, W. Huang, H. Fu, J. Kim, Z. Wei, M. Flavin, J. McCracken, R. Wang, A. Badea, Y. Liu, D. Xiao, G. Zhou, J. Lee, H. U. Chung, H. Cheng, W. Ren, A. Banks, X. Li, U. Paik, R. G. Nuzzo, Y. Huang, Y. Zhang, J. A. Rogers, *Science* **2015**, *347*, 154.
- [140] Z. Yan, M. Han, Y. Yang, K. Nan, H. Luan, Y. Luo, Y. Zhang, Y. Huang, J. A. Rogers, *Extreme Mech. Lett.* **2017**, *11*, 96.
- [141] Y. Liu, Z. Yan, Q. Lin, X. Guo, M. Han, K. Nan, K. C. Hwang, Y. Huang, Y. Zhang, J. A. Rogers, *Adv. Funct. Mater.* **2016**, *26*, 2909.
- [142] K. I. Jang, K. Li, H. U. Chung, S. Xu, H. N. Jung, Y. Yang, J. W. Kwak, H. H. Jung, J. Song, C. Yang, A. Wang, Z. Liu, J. Y. Lee, B. H. Kim, J. H. Kim, J. Lee, Y. Yu, B. J. Kim, H. Jang, K. J. Yu, J. Kim, J. W. Lee, J. W. Jeong, Y. M. Song, Y. Huang, Y. Zhang, J. A. Rogers, *Nat. Commun.* **2017**, *8*, 15894.
- [143] H. Jinno, K. Fukuda, X. Xu, S. Park, Y. Suzuki, M. Koizumi, T. Yokota, I. Osaka, K. Takimiya, T. Someya, *Nat. Energy* **2017**, *2*, 780.
- [144] J. Viventi, D. H. Kim, L. Vigeland, E. S. Frechette, J. A. Blanco, Y. S. Kim, A. E. Avrin, V. R. Tiruvadi, S. W. Hwang, A. C. Vanleer, D. F. Wulsin, K. Davis, C. E. Gelber, L. Palmer, J. Van der Spiegel, J. Wu, J. Xiao, Y. Huang, D. Contreras, J. A. Rogers, B. Litt, *Nat. Neurosci.* **2011**, *14*, 1599.
- [145] F. Sorgini, A. Mazzoni, L. Massari, R. Calio, C. Galassi, S. L. Kukreja, E. Sinibaldi, M. C. Carozza, C. M. Oddo, *Micromachines* **2017**, *8*, 270.
- [146] K. Li, X. Cheng, F. Zhu, L. Li, Z. Xie, H. Luan, Z. Wang, Z. Ji, H. Wang, F. Liu, Y. Xue, C. Jiang, X. Feng, L. Li, J. A. Rogers, Y. Huang, Y. Zhang, *Adv. Funct. Mater.* **2019**, *29*, 1805615.
- [147] Y. H. Zhang, H. R. Fu, Y. W. Su, S. Xu, H. Y. Cheng, J. A. Fan, K. C. Hwang, J. A. Rogers, Y. G. Huang, *Acta Mater.* **2013**, *61*, 7816.
- [148] S. Xu, Y. Zhang, J. Cho, J. Lee, X. Huang, L. Jia, J. A. Fan, Y. Su, J. Su, H. Zhang, H. Cheng, B. Lu, C. Yu, C. Chuang, T. I. Kim, T. Song, K. Shigeta, S. Kang, C. Dagdeviren, I. Petrov, P. V. Braun, Y. Huang, U. Paik, J. A. Rogers, *Nat. Commun.* **2013**, *4*, 1543.
- [149] Y. Zhang, H. Fu, S. Xu, J. A. Fan, K.-C. Hwang, J. Jiang, J. A. Rogers, Y. Huang, *J. Mech. Phys. Solids* **2014**, *72*, 115.
- [150] Y. Su, S. Wang, Y. Huang, H. Luan, W. Dong, J. A. Fan, Q. Yang, J. A. Rogers, Y. Huang, *Small* **2015**, *11*, 367.
- [151] Q. Ma, Y. Zhang, *J. Appl. Mech.* **2016**, *83*, 111008.
- [152] L. Xu, S. R. Gutbrod, Y. Ma, A. Petrossians, Y. Liu, R. C. Webb, J. A. Fan, Z. Yang, R. Xu, J. J. Whalen 3rd, J. D. Weiland, Y. Huang, I. R. Efimov, J. A. Rogers, *Adv. Mater.* **2015**, *27*, 1731.
- [153] J. J. Norton, D. S. Lee, J. W. Lee, W. Lee, O. Kwon, P. Won, S. Y. Jung, H. Cheng, J. W. Jeong, A. Akce, S. Umunna, I. Na, Y. H. Kwon, X. Q. Wang, Z. Liu, U. Paik, Y. Huang, T. Bretl, W. H. Yeo, J. A. Rogers, *Proc. Natl. Acad. Sci. USA* **2015**, *112*, 3920.
- [154] J. A. Fan, W. H. Yeo, Y. Su, Y. Hattori, W. Lee, S. Y. Jung, Y. Zhang, Z. Liu, H. Cheng, L. Falgout, M. Bajema, T. Coleman, D. Gregoire, R. J. Larsen, Y. Huang, J. A. Rogers, *Nat. Commun.* **2014**, *5*, 3266.
- [155] J. Kim, M. Lee, H. J. Shim, R. Ghaffari, H. R. Cho, D. Son, Y. H. Jung, M. Soh, C. Choi, S. Jung, K. Chu, D. Jeon, S.-T. Lee, J. H. Kim, S. H. Choi, T. Hyeon, D.-H. Kim, *Nat. Commun.* **2014**, *5*, 5747.
- [156] Y. Hattori, L. Falgout, W. Lee, S. Y. Jung, E. Poon, J. W. Lee, I. Na, A. Geisler, D. Sathwani, Y. Zhang, Y. Su, X. Wang, Z. Liu, J. Xia, H. Cheng, R. C. Webb, A. P. Bonifas, P. Won, J. W. Jeong, K. I. Jang, Y. M. Song, B. Nardone, M. Nodzenski, J. A. Fan, Y. Huang, D. P. West, A. S. Paller, M. Alam, W. H. Yeo, J. A. Rogers, *Adv. Healthcare Mater.* **2014**, *3*, 1597.
- [157] Y. Tang, G. Lin, S. Yang, Y. K. Yi, R. D. Kamien, J. Yin, *Adv. Mater.* **2017**, *29*.
- [158] M. Eidini, *Extreme Mech. Lett.* **2016**, *6*, 96.
- [159] L. Xu, T. C. Shyu, N. A. Kotov, *ACS Nano* **2017**, *11*, 7587.
- [160] A. Rafsanjani, K. Bertoldi, *Phys. Rev. Lett.* **2017**, *118*, 084301.
- [161] S. J. P. Callens, A. A. Zadpoor, *Mater. Today* **2018**, *21*, 241.
- [162] T. C. Shyu, P. F. Damasceno, P. M. Dodd, A. Lamoureux, L. Xu, M. Shlian, M. Shtein, S. C. Glotzer, N. A. Kotov, *Nat. Mater.* **2015**, *14*, 785.
- [163] A. Lamoureux, K. Lee, M. Shlian, S. R. Forrest, M. Shtein, *Nat. Commun.* **2015**, *6*, 8092.
- [164] L. Xu, X. Wang, Y. Kim, T. C. Shyu, J. Lyu, N. A. Kotov, *ACS Nano* **2016**, *10*, 6156.
- [165] Y. Morikawa, S. Yamagiwa, H. Sawahata, R. Numano, K. Koida, M. Ishida, T. Kawano, *Adv. Healthcare Mater.* **2018**, *7*, 1701100.
- [166] Z. Song, X. Wang, C. Lv, Y. An, M. Liang, T. Ma, D. He, Y. J. Zheng, S. Q. Huang, H. Yu, H. Jiang, *Sci. Rep.* **2015**, *5*, 10988.
- [167] M. K. Blees, A. W. Barnard, P. A. Rose, S. P. Roberts, K. L. McGill, P. Y. Huang, A. R. Ruyack, J. W. Kevek, B. Kobrin, D. A. Muller, P. L. McEuen, *Nature* **2015**, *524*, 204.
- [168] H. Seifi, A. R. Javan, A. Ghaedizadeh, J. Shen, S. Xu, Y. M. Xie, *Sci. Rep.* **2017**, *7*, 41183.
- [169] Y. Tang, G. Lin, L. Han, S. Qiu, S. Yang, J. Yin, *Adv. Mater.* **2015**, *27*, 7181.
- [170] R. Gatt, L. Mizzi, J. I. Azzopardi, K. M. Azzopardi, D. Attard, A. Casha, J. Briffa, J. N. Grima, *Sci. Rep.* **2015**, *5*, 8395.
- [171] J. N. Grima, K. E. Evans, *J. Mater. Sci. Lett.* **2000**, *19*, 1563.
- [172] K. Bertoldi, V. Vitelli, J. Christensen, M. van Hecke, *Nat. Rev. Mater.* **2017**, *2*, 17066.
- [173] Y. C. Tang, J. Yin, *Extreme Mech. Lett.* **2017**, *12*, 77.
- [174] J. A. Wu, M. Li, W. Q. Chen, D. H. Kim, Y. S. Kim, Y. G. Huang, K. C. Hwang, Z. Kang, J. A. Rogers, *Acta Mech. Sin.* **2010**, *26*, 881.
- [175] H. Li, Z. Wang, S. Lu, Y. Ma, X. Feng, *Adv. Mater. Technol.* **2019**, *4*, 1800365.
- [176] J. Lee, J. Wu, M. Shi, J. Yoon, S. I. Park, M. Li, Z. Liu, Y. Huang, J. A. Rogers, *Adv. Mater.* **2011**, *23*, 986.
- [177] S. Biswas, J. Reiprich, T. Cohrs, D. T. Arboleda, A. Schoeberl, M. Mozafari, L. Schlag, T. Stauden, J. Pezoldt, H. O. Jacobs, *Adv. Mater. Technol.* **2017**, *2*, 1700131.
- [178] R. Libanori, R. M. Erb, A. Reiser, H. Le Ferrand, M. J. Sues, R. Spolenak, A. R. Studart, *Nat. Commun.* **2012**, *3*, 1265.
- [179] Y. K. Lee, K. I. Jang, Y. Ma, A. Koh, H. Chen, H. N. Jung, Y. Kim, J. W. Kwak, L. Wang, Y. Xue, Y. Yang, W. Tian, Y. Jiang, Y. Zhang, X. Feng, Y. Huang, J. A. Rogers, *Adv. Funct. Mater.* **2017**, *27*, 1605476.
- [180] D. H. Kim, N. Lu, R. Ghaffari, Y. S. Kim, S. P. Lee, L. Xu, J. Wu, R. H. Kim, J. Song, Z. Liu, J. Viventi, B. de Graff, B. Elolamp, M. Mansour, M. J. Slepian, S. Hwang, J. D. Moss, S. M. Won, Y. Huang, B. Litt, J. A. Rogers, *Nat. Mater.* **2011**, *10*, 316.
- [181] H. Vandeparre, Q. Liu, I. R. Mineev, Z. Suo, S. P. Lacour, *Adv. Mater.* **2013**, *25*, 3117.

- [182] T. Takahashi, K. Takei, A. G. Gillies, R. S. Fearing, A. Javey, *Nano Lett.* **2011**, *11*, 5408.
- [183] Z. Liu, H. Cheng, J. Wu, *J. Appl. Mech.* **2014**, *81*, 044501.
- [184] J. Lee, J. Wu, J. H. Ryu, Z. Liu, M. Meitl, Y. W. Zhang, Y. Huang, J. A. Rogers, *Small* **2012**, *8*, 1851.
- [185] G. Cantarella, V. Costanza, A. Ferrero, R. Hopf, C. Vogt, M. Varga, L. Petti, N. Munzenrieder, L. Buthe, G. Salvatore, A. Claville, L. Bonanomi, A. Daus, S. Knobelspies, C. Daraio, G. Troster, *Adv. Funct. Mater.* **2018**, *28*, 1705132.
- [186] Q. Zhao, Z. W. Liang, B. W. Lu, Y. Chen, Y. J. Ma, X. Feng, *Adv. Mater. Technol.* **2018**, *3*, 1800169.
- [187] H. Zhou, W. Qin, Q. Yu, F. Chen, X. Yu, H. Cheng, H. Wu, *Int. J. Solids Struct.* **2019**, *160*, 96.
- [188] Q. M. Yu, F. R. Chen, M. Li, H. Y. Cheng, *Appl. Phys. Lett.* **2017**, *111*, 202406.
- [189] D. Qi, Z. Liu, M. Yu, Y. Liu, Y. Tang, J. Lv, Y. Li, J. Wei, B. Liedberg, Z. Yu, X. Chen, *Adv. Mater.* **2015**, *27*, 3145.
- [190] D. Qi, Z. Liu, Y. Liu, W. R. Leow, B. Zhu, H. Yang, J. Yu, W. Wang, H. Wang, S. Yin, X. Chen, *Adv. Mater.* **2015**, *27*, 5559.
- [191] F. Zhu, H. Xiao, H. Li, Y. Huang, Y. Ma, *J. Appl. Mech.* **2018**.
- [192] H. Chen, F. Zhu, K. I. Jang, X. Feng, J. A. Rogers, Y. Zhang, Y. Huang, Y. Ma, *J. Mech. Phys. Solids* **2018**, *120*, 199.
- [193] Q. Ma, H. Cheng, K. I. Jang, H. Luan, K. C. Hwang, J. A. Rogers, Y. Huang, Y. Zhang, *J. Mech. Phys. Solids* **2016**, *90*, 179.
- [194] E. Zhang, Y. Liu, Y. Zhang, *J. Appl. Mech.* **2018**, *85*, 071002.
- [195] J. Liu, Y. Zhang, *J. Appl. Mech.* **2018**, *85*, 051003.
- [196] J. Liu, Y. Zhang, *Soft Matter* **2018**, *14*, 693.
- [197] M. Ying, A. P. Bonifas, N. Lu, Y. Su, R. Li, H. Cheng, A. Ameen, Y. Huang, J. A. Rogers, *Nanotechnology* **2012**, *23*, 344004.
- [198] C. D. Petruczuk, K. K. Gleason, *Adv. Mater.* **2012**, *24*, 6445.
- [199] C. Yu, Z. Duan, P. Yuan, Y. Li, Y. Su, X. Zhang, Y. Pan, L. L. Dai, R. G. Nuzzo, Y. Huang, H. Jiang, J. A. Rogers, *Adv. Mater.* **2013**, *25*, 1541.
- [200] A. M. Bowen, R. G. Nuzzo, *Adv. Funct. Mater.* **2009**, *19*, 3243.
- [201] I. Jung, G. Shin, V. Malyarchuk, J. S. Ha, J. A. Rogers, *Appl. Phys. Lett.* **2010**, *96*, 021110.
- [202] G. Shin, I. Jung, V. Malyarchuk, J. Song, S. Wang, H. C. Ko, Y. Huang, J. S. Ha, J. A. Rogers, *Small* **2010**, *6*, 851.
- [203] S. Wang, J. Xiao, I. Jung, J. Song, H. C. Ko, M. P. Stoykovich, Y. Huang, K.-C. Hwang, J. A. Rogers, *Appl. Phys. Lett.* **2009**, *95*, 181912.
- [204] I. Jung, J. Xiao, V. Malyarchuk, C. Lu, M. Li, Z. Liu, J. Yoon, Y. Huang, J. A. Rogers, *Proc. Natl. Acad. Sci. USA* **2011**, *108*, 1788.
- [205] C. Lü, M. Li, J. Xiao, I. Jung, J. Wu, Y. Huang, K.-C. Hwang, J. A. Rogers, *J. Appl. Mech.* **2013**, *80*, 061022.
- [206] Y. W. Su, Z. J. Liu, S. D. Wang, R. Ghaffari, D. H. Kim, K. C. Hwang, J. A. Rogers, Y. G. Huang, *Int. J. Solids Struct.* **2014**, *51*, 1555.
- [207] S. P. Lee, L. E. Klinker, L. Ptaszek, J. Work, C. Liu, F. Quivara, C. Webb, C. Dagdeviren, J. A. Wright, J. N. Ruskin, M. Slepian, Y. Huang, M. Mansour, J. A. Rogers, R. Ghaffari, *Proc. IEEE* **2015**, *103*, 682.
- [208] D. H. Kim, R. Ghaffari, N. Lu, S. Wang, S. P. Lee, H. Keum, R. D'Angelo, L. Klinker, Y. Su, C. Lu, Y. S. Kim, A. Ameen, Y. Li, Y. Zhang, B. de Graff, Y. Y. Hsu, Z. Liu, J. Ruskin, L. Xu, C. Lu, F. G. Omenetto, Y. Huang, M. Mansour, M. J. Slepian, J. A. Rogers, *Proc. Natl. Acad. Sci. USA* **2012**, *109*, 19910.
- [209] S. A. Zirbel, R. J. Lang, M. W. Thomson, D. A. Sigel, P. E. Walkemeyer, B. P. Trease, S. P. Magleby, L. L. Howell, *J. Mech. Des.* **2013**, *135*, 111005.
- [210] X. Ning, X. Wang, Y. Zhang, X. Yu, D. Choi, N. Zheng, D. S. Kim, Y. Huang, Y. Zhang, J. A. Rogers, *Adv. Mater. Interfaces* **2018**, *5*, 1800284.
- [211] Z. Liu, A. Cui, J. Li, C. Gu, *Adv. Mater.* **2018**, *31*, e1802211.
- [212] Z. Zhao, X. Kuang, J. Wu, Q. Zhang, G. H. Paulino, H. J. Qi, D. Fang, *Soft Matter* **2018**, *14*, 8051.
- [213] S. Felton, M. Tolley, E. Demaine, D. Rus, R. Wood, *Science* **2014**, *345*, 644.
- [214] K. Kuribayashi, K. Tsuchiya, Z. You, D. Tomus, M. Umemoto, T. Ito, M. Sasaki, *Mater. Sci. Eng., A* **2006**, *419*, 131.
- [215] J.-H. Cho, M. D. Keung, N. Verellen, L. Lagae, V. V. Moshchalkov, P. Van Dorpe, D. H. Gracias, *Small* **2011**, *7*, 1943.
- [216] Z. Song, C. Lv, M. Liang, V. Sanphuang, K. Wu, B. Chen, Z. Zhao, J. Bai, X. Wang, J. L. Volakis, L. Wang, X. He, Y. Yao, S. Tongay, H. Jiang, *Small* **2016**, *12*, 5401.
- [217] M. Z. Miskin, K. J. Dorsey, B. Bircan, Y. Han, D. A. Muller, P. L. McEuen, I. Cohen, *Proc. Natl. Acad. Sci. USA* **2018**, *115*, 466.
- [218] V. B. Shenoy, D. H. Gracias, *MRS Bull.* **2012**, *37*, 847.
- [219] C. Yang, Y. Huang, H. Cheng, L. Jiang, L. Qu, *Adv. Mater.* **2019**, *31*, 1805705.
- [220] R. Tang, H. Huang, H. E. Tu, H. S. Liang, M. B. Liang, Z. M. Song, Y. Xu, H. Q. Jiang, H. Y. Yu, *Appl. Phys. Lett.* **2014**, *104*, 083501.
- [221] J. P. Rojas, D. Conchouso, A. Arevalo, D. Singh, I. G. Foulds, M. M. Hussain, *Nano Energy* **2017**, *31*, 296.
- [222] P.-K. Yang, Z.-H. Lin, K. C. Pradel, L. Lin, X. Li, X. Wen, J.-H. He, Z. L. Wang, *ACS Nano* **2015**, *9*, 901.
- [223] M. Kim, J. Park, S. Ji, S. H. Shin, S. Y. Kim, Y. C. Kim, J. Y. Kim, J. U. Park, *Nanoscale* **2016**, *8*, 9504.
- [224] S. Ji, B. G. Hyun, K. Kim, S. Y. Lee, S. H. Kim, J. Y. Kim, M. H. Song, J. U. Park, *NPG Asia Mater.* **2016**, *8*, e299.
- [225] M. Schenk, S. D. Guest, *Proc. Natl. Acad. Sci. USA* **2013**, *110*, 3276.
- [226] Q. Cheng, Z. Song, T. Ma, B. B. Smith, R. Tang, H. Yu, H. Jiang, C. K. Chan, *Nano Lett.* **2013**, *13*, 4969.
- [227] C. H. Lin, D. S. Tsai, T. C. Wei, D. H. Lien, J. J. Ke, C. H. Su, J. Y. Sun, Y. C. Liao, J. H. He, *ACS Nano* **2017**, *11*, 10230.
- [228] K. Zhang, Y. H. Jung, S. Mikael, J. H. Seo, M. Kim, H. Mi, H. Zhou, Z. Xia, W. Zhou, S. Gong, Z. Ma, *Nat. Commun.* **2017**, *8*, 1782.
- [229] Y. Shi, F. Zhang, K. Nan, X. Wang, J. Wang, Y. Zhang, Y. Zhang, H. Luan, K. C. Hwang, Y. Huang, J. A. Rogers, Y. Zhang, *Extreme Mech. Lett.* **2017**, *11*, 105.
- [230] Y. Zhang, F. Zhang, Z. Yan, Q. Ma, X. Li, Y. Huang, J. A. Rogers, *Nat. Rev. Mater.* **2017**, *2*, 17019.
- [231] W. Lee, Y. Liu, Y. Lee, B. K. Sharma, S. M. Shinde, S. D. Kim, K. Nan, Z. Yan, M. Han, Y. Huang, Y. Zhang, J.-H. Ahn, J. A. Rogers, *Nat. Commun.* **2018**, *9*, 1417.
- [232] X. Guo, X. Wang, D. Ou, J. Ye, W. Pang, Y. Huang, J. A. Rogers, Y. Zhang, *npj Flexible Electron.* **2018**, *2*, 14.
- [233] J. J. Adams, E. B. Duoss, T. F. Malkowski, M. J. Motala, B. Y. Ahn, R. G. Nuzzo, J. T. Bernhard, J. A. Lewis, *Adv. Mater.* **2011**, *23*, 1335.
- [234] C. Pfeiffer, X. Xu, S. R. Forrest, A. Grbic, *Adv. Mater.* **2012**, *24*, 1166.
- [235] Z. Wu, M. Jobs, A. Rydberg, K. Hjort, *J. Micromech. Microeng.* **2015**, *25*, 027004.
- [236] F. Liu, Y. Chen, H. Song, F. Zhang, Z. Fan, Y. Liu, X. Feng, J. A. Rogers, Y. Huang, Y. Zhang, *Small* **2019**, *15*, 1804055.
- [237] M. Jobs, K. Hjort, A. Rydberg, Z. Wu, *Small* **2013**, *9*, 3230.
- [238] S. R. Best, D. L. Hanna, *IEEE Antennas Propag. Mag.* **2010**, *52*, 47.
- [239] H. Fu, K. Nan, W. Bai, W. Huang, K. Bai, L. Lu, C. Zhou, Y. Liu, F. Liu, J. Wang, M. Han, Z. Yan, H. Luan, Y. Zhang, Y. Zhang, J. Zhao, X. Cheng, M. Li, J. W. Lee, Y. Liu, D. Fang, X. Li, Y. Huang, Y. Zhang, J. A. Rogers, *Nat. Mater.* **2018**, *17*, 268.
- [240] B. H. Kim, F. Liu, Y. Yu, H. Jang, Z. Xie, K. Li, J. Lee, J. Y. Jeong, A. Ryu, Y. Lee, D. H. Kim, X. Wang, K. Lee, J. Y. Lee, S. M. Won, N. Oh, J. Kim, J. Y. Kim, S.-J. Jeong, K.-I. Jang, S. Lee, Y. Huang, Y. Zhang, J. A. Rogers, *Adv. Funct. Mater.* **2018**, *28*, 1803149.
- [241] Y. Ling, X. Zhuang, Z. Xu, Y. Xie, X. Zhu, Y. Xu, B. Sun, J. Lin, Y. Zhang, Z. Yan, *ACS Nano* **2018**, *12*, 12456.
- [242] B. H. Kim, J. Lee, S. M. Won, Z. Xie, J.-K. Chang, Y. Yu, Y. K. Cho, H. Jang, J. Y. Jeong, Y. Lee, A. Ryu, D. H. Kim, K. H. Lee, J. Y. Lee, F. Liu, X. Wang, Q. Huo, S. Min, D. Wu, B. Ji, A. Banks, J. Kim, N. Oh, H. M. Jin, S. Han, D. Kang, C. H. Lee, Y. M. Song, Y. Zhang, Y. Huang, K.-I. Jang, J. A. Rogers, *ACS Nano* **2018**, *12*, 4164.

- [243] R. Xu, J. W. Lee, T. Pan, S. Ma, J. Wang, J. H. Han, Y. Ma, J. A. Rogers, Y. Huang, *Adv. Funct. Mater.* **2017**, *27*, 1604545.
- [244] R.-H. Kim, D.-H. Kim, J. Xiao, B. H. Kim, S.-I. Park, B. Panilaitis, R. Ghaffari, J. Yao, M. Li, Z. Liu, V. Malyarchuk, D. G. Kim, A.-P. Le, R. G. Nuzzo, D. L. Kaplan, F. G. Omenetto, Y. Huang, Z. Kang, J. A. Rogers, *Nat. Mater.* **2010**, *9*, 929.
- [245] J. W. Lee, R. Xu, S. Lee, K.-I. Jang, Y. Yang, A. Banks, K. J. Yu, J. Kim, S. Xu, S. Ma, S. W. Jang, P. Won, Y. Li, B. H. Kim, J. Y. Choe, S. Huh, Y. H. Kwon, Y. Huang, U. Paik, J. A. Rogers, *Proc. Natl. Acad. Sci. USA* **2016**, *113*, 6131.
- [246] Z. Huang, Y. Hao, Y. Li, H. Hu, C. Wang, A. Nomoto, T. Pan, Y. Gu, Y. Chen, T. Zhang, W. Li, Y. Lei, N. Kim, C. Wang, L. Zhang, J. W. Ward, A. Maralani, X. Li, M. F. Durstock, A. Pisano, Y. Lin, S. Xu, *Nat. Electron.* **2018**, *1*, 473.
- [247] C. Wang, C. Wang, Z. Huang, S. Xu, *Adv. Mater.* **2018**, *30*, 1801368.
- [248] Y. Huang, H. Wu, L. Xiao, Y. Duan, H. Zhu, J. Bian, D. Ye, Z. Yin, *Mater. Horiz.* **2019**, *6*, 642.
- [249] S. Wagner, S. Bauer, *MRS Bull.* **2012**, *37*, 207.
- [250] T. R. Ray, J. Choi, A. J. Bandodkar, S. Krishnan, P. Gutruf, L. Tian, R. Ghaffari, J. A. Rogers, *Chem. Rev.* **2019**, *119*, 5461.
- [251] S. Choi, H. Lee, R. Ghaffari, T. Hyeon, D.-H. Kim, *Adv. Mater.* **2016**, *28*, 4203.
- [252] G. C. Engelmayr Jr., M. Cheng, C. J. Bettinger, J. T. Borenstein, R. Langer, L. E. Freed, *Nat. Mater.* **2008**, *7*, 1003.